Theoretical derivation and a priori validation of a new scalar variance-based sub-grid drag force model for simulation of gas–solid fluidized beds

Baptiste Hardy, Pascal Fede, Olivier Simonin

Powder Technology 436 (2024) 119454

Contents lists available at ScienceDirect

Powder Technology

journal homepage: www.journals.elsevier.com/powder-technology

Theoretical derivation and *a priori* validation of a new scalar variance-based sub-grid drag force model for simulation of gas–solid fluidized beds

Baptiste Hardy *, Pascal Fede, Olivier Simonin

Institut de Mécanique des Fluides de Toulouse (IMFT), Université de Toulouse, CNRS, France

HIGHLIGHTS

- Sub-grid drag modeling is needed for large-scale simulation of fluidized beds.
- A theoretical drift velocity model is derived from a transport equation.
- Sub-grid moments of the solid volume fraction are closed by a large-eddy PDF approach.
- A scalar-variance based functional model is proposed and validated for Geldart A and B particles.

GRAPHICAL ABSTRACT

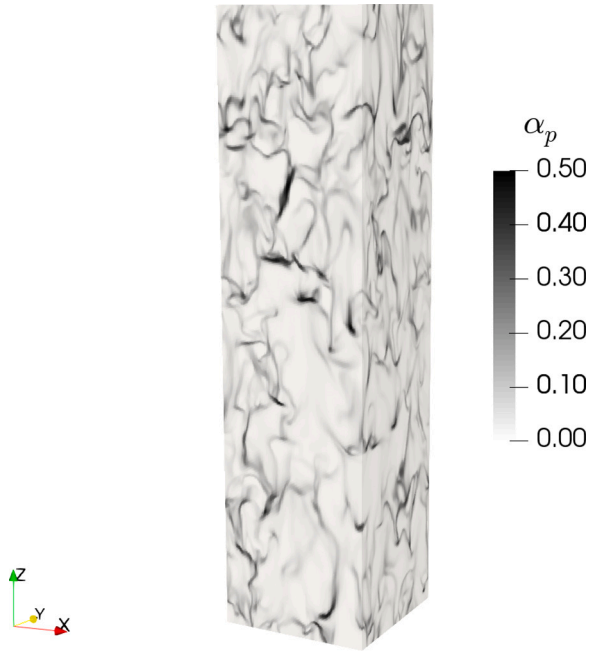

ARTICLE INFO

Keywords:
Euler–Euler model
Sub-grid drag force model
Coarse-grain modeling
Scalar variance
Large-eddy PDF
Fluidized beds

ABSTRACT

A novel sub-grid drag force model is proposed for coarse-grid Euler–Euler simulation of gas–solid fluidized beds. Starting from a transport equation for the drift velocity, an equilibrium condition is used as a basis to derive a new algebraic drift velocity model. The sub-grid correlations that show up are closed by a large-eddy PDF approach inspired from LES of turbulent reacting flows. The new analytical model only depends on the resolved slip velocity and on a few sub-grid moments of the solid volume fraction. Then, a conditional averaging procedure shows that the new model can be properly captured by a simple functional expression that only requires a closure for the sub-grid variance of the solid volume fraction. *A priori* validation studies show that the drift velocity is predicted with high accuracy ($R^2 > 0.90$) for a large range of filter widths and for both Geldart A and Geldart B particles.

* Corresponding author.
E-mail address: baptiste.hardy@imft.fr (B. Hardy).

https://doi.org/10.1016/j.powtec.2024.119454
Received 3 August 2023; Received in revised form 27 November 2023; Accepted 21 January 2024
Available online 23 January 2024

1. Introduction

Gas–solid flows are encountered in numerous environmental phenomena and industrial applications, including Fluid Catalytic Cracking (FCC), Chemical Looping Combustion (CLC) or biomass conversion. A detailed comprehension of the hydrodynamics of these processes proves to be crucial to optimize their performance and ensure safety during operation. In the past decades, Computational Fluid Dynamics has been increasingly used to gain a more fundamental understanding of the complex flows that govern the dynamics of gas–solid fluidized beds. Among the existing methods (see [1] for a review) the Euler–Euler model has been successfully employed for systems implying billions of particles [2]. In this approach, the fluid and the solid phases are treated as interpenetrating continua. Distinct transport equations are solved for each phase and the closures for the particulate stress term are commonly derived from the kinetic theory of granular flows (KTGF) [3–5].

As a result of the non-linear fluid–particle interactions and inelastic particle–particle and particle–wall collisions, instabilities will arise in the form of bubbles (large voids of particles) in bubbling fluidized beds (BFB) or clusters and streamers of particles in circulating fluidized beds (CFB) [6–8]. These mesoscale structures have been observed experimentally [9,10] and can be properly captured with a Eulerian approach in relatively small domains and with fine computational grids. In industrial cases, however, these structures will span over a large range of length scales, from a few particle diameters to the size of the vessel. This makes fully resolved ('fine-grid') Euler–Euler simulations still out of reach for industrial-scale units. As coarse grids must be used, mesoscale structures smaller than the mesh size will be filtered out. However, a number of previous works [6,7,11–15] showed that, in the absence of sub-grid modeling, coarse-grid Euler–Euler simulations fail to capture even the global features of the bed, highlighting the impact of these mesoscale structures on the macroscale hydrodynamics. For Geldart A particles, it is now well established that omitting the contribution of the sub-grid fluid–particle drag force term leads to a gross overestimation of the bed height in dense bubbling fluidized beds or of the solids circulation rate in dilute circulating fluidized beds.

Over the last decades, different methods have emerged in the literature to account for the impact of the sub-grid scale structures on the resolved part of the flow in coarse-grid simulations. Given its primary importance, most efforts targeted the modeling of the sub-grid drag force term, although some authors also investigated closures for the mesoscale particulate stresses, usually by analogy with existing turbulence models in single phase flows [15,16]. In what follows, we will only provide an overview of the various approaches proposed in the literature to model the sub-grid drag force term. The interested reader is referred to [7,17] for more extensive reviews.

Drag correlations accounting for heterogeneities at the sub-grid scale were first proposed by O'Brien et al. [18] Later on, different authors suggested to use a scaling factor between 0 and 1 to reduce the effective drag force with respect to the homogeneous case [19–21]. By using ad-hoc calibration, these authors assigned a constant value to this scaling factor over the whole bed. For bubbling fluidized beds of Geldart B particles, Wang et al. [13] proposed a bubble-emulsion model where all the drag force is assumed to be contained within the dense emulsion phase. Empirical correlations are then used to determine the solid volume fraction and the slip velocity in the dense phase in order to compute the effective drag force. In the EMMS model originally proposed by Li and Kwauk [22], particles are assumed to be homogeneously distributed inside and outside the clusters. The solution to the many unknowns of the problem (volume fraction and phase velocities inside and outside the clusters, clustering fraction, . . .) results from the minimization of the suspension energy. Since then, the EMMS approach has been employed for coarse-grid Eulerian simulations of various fluidized systems [23,24].

In the last years, most studies focused on deriving closures for the sub-grid drag force term by filtering very fine-grid simulation data. By analogy with Large Eddy Simulations (LES) in single phase flows, a low-pass filter is applied to the governing equations of the 'microscale' Euler–Euler model in order to identify the filtered and sub-grid terms in coarse-grid simulations. Based on fine-grid 2-D simulations of a riser flow, Andrews et al. [11] suggested to model the instantaneous mesoscale drag coefficient as the sum of a deterministic and a stochastic contributions. Following this study, Igci et al. [12] and Igci and Sundaresan [16] proposed to model the drag law scaling factor as a function of the filter size and the filtered solid volume fraction, thereby overcoming previous attempts that considered this scaling factor as uniform over the entire bed. Their model was later validated against experimental data in 3-D riser flows [25]. Milioli et al. [26] suggested that the correction factor should have an additional dependence on the filtered slip velocity. Sarkar et al. [27] proposed new closures for the filtered drag force and the mesoscale stresses and performed validation tests in large-scale bubbling fluidized beds. Later, both Cloete al. [28] and Gao et al. [29] performed comparative studies of the various filtered Euler–Euler models proposed in the literature over a wide range of fluidization regimes. In parallel, Parmentier et al. [14] identified the link between the overestimation of the effective drag force term in coarse-grid simulations and the existence of a drift velocity at the sub-grid scale. Based on fine-grid Euler–Euler simulations of 2-D BFB, these authors proposed a functional model for the drift velocity that depends on the filter size, the filtered volume fraction and the resolved slip velocity. The originality of their work also lies in the use of Germano's dynamic procedure [30] to adjust the model constant. Based on refined simulations of wall-bounded CFB, Ozel et al. [15] adapted the drift velocity model proposed in [14] to this three-dimensional case and investigated new structural models inspired from Large Eddy Simulations in single phase turbulence. Besides, the concept of drift velocity has been adopted in the Reynolds-averaged theory of gas–solid flows, where it appears as a source of the so-called 'cluster-induced' turbulence [31–33]. More recently, Schneiderbauer [34] introduced a new spatially-averaged two-fluid model (SA-TFM) where the filtered drag force is closed using series expansion of the microscopic drag coefficient. The sub-grid correlations that appear in this model are expressed as functions of the sub-grid correlated kinetic energy of both phases and of the sub-grid variance of the solid volume fraction. With the same kind of approach, Rauchenzauner and Schneiderbauer [35] proposed an anisotropic model for the drift velocity, requiring additional transport equations for the mesoscale stresses of each phase. This model was verified *a posteriori* in wall-bounded fluidization of Geldart A and Geldart B particles [36]. Ozel et al. [37] argued that the drift velocity scaled by the resolved slip velocity might not be sufficient to fully capture the drag correction. Therefore, they suggested to add the sub-grid variance of the solid volume fraction as a second marker to improve the performance of the model. They also pointed out that the accuracy of the closures used for these sub-grid quantities (drift velocity and scalar variance) is the most crucial factor for the reliability of the final model. In parallel, Jiang et al. [38] derived a transport equation for the drift velocity itself in order to inform a neural network procedure. They came to the conclusion that using the resolved gas phase pressure gradient in addition to the resolved slip velocity produced better results. Their model was validated *a posteriori* in coarse-grid simulations of a bubbling fluidized bed of Geldart A particles and later extended to other physical parameters [39].

The various methods presented above have been successfully applied to different fluidized systems, but most of them present one the these two drawbacks: (i) they rely on an ad-hoc calibration, diminishing the reliability of their use for other types of particles or fluidization regimes, or (ii) they require a number of additional transport equations, increasing the computational cost and shifting the modeling difficulty to new unclosed terms. In this work, our goal is to build a new drift

Table 1
Physical and geometrical parameters used in fine-grid simulations of a tri-periodic fluidized bed of Geldart A particles.

Particle diameter d_p	75 μm
Particle density ρ_p	1500 kg/m^3
Average solid volume fraction $\{\alpha_p\}$	0.05
Restitution coefficient e_c	0.9
Gas density ρ_g	1.2 kg/m^3
Gas dynamic viscosity μ_g	1.8×10^{-5} Pa s
Terminal velocity U_t	0.219 m/s
Vertical dimension L_z	0.1536 m
Horizontal dimension $L_x = L_y$	0.0384 m
Grid size Δ	240 μm
Fr_p	65.33
Fr_Δ	20.41

velocity model based on physical grounds, with a minimal number of additional transport equations.

The structure of this article is the following. Section 2 presents the numerical set-up used to perform fine-grid Euler–Euler simulations of a tri-periodic fluidized bed. In Section 3, a transport equation is derived for the drift velocity and a local equilibrium condition is identified. Section 4 details how this equilibrium condition coupled with as large-eddy PDF approach is used to derive a new algebraic drift velocity model. In Section 5, a conditional averaging procedure reveals that the new model can be very well approximated by a function of the first two sub-grid moments of the particle volume fraction, i.e. the filtered value and the sub-grid variance. A functional drift velocity model is proposed and validated for Geldart A and Geldart B particles. Finally, Section 6 summarizes the main outcomes of this work and discusses future research directions.

2. Numerical set-up

To characterize the influence of the sub-grid scale structures on the resolved scales of the flow in coarse-grid simulations, we performed fine-grid (i.e. mesh independent) simulations of a tri-periodic fluidized bed using the multi-fluid CFD software *neptune_cfd* (see [2] for a recent demonstration of its capabilities). The details of the mathematical model are provided in previous works [14,15] and recalled in Appendix A. The gravitational acceleration is given by $\mathbf{g} = -9.81\mathbf{e}_z$, and an external momentum forcing term is added in the vertical direction to compensate for the weight of the mixture. The physical parameters of a typical air–FCC system are summarized in Table 1, where are also introduced the terminal settling velocity U_t and the characteristic Froude numbers based on the particle diameter, $Fr_p = \frac{U_t^2}{g d_p}$, and on the grid size, $Fr_\Delta = \frac{U_t^2}{g\Delta}$. The grid is uniform in the three directions with $n_z = 640$ cells along the vertical dimension and the aspect ratio between the vertical and horizontal dimensions L_z/L_x is 4. Statistics are collected over 5 s once the flow has reached a statistically steady state. The particle clusters that result from the non-linear gas–solid interactions and from the non-elastic collisions are clearly identified in Fig. 1, showing a snapshot of the particle volume fraction field α_p. The resolution of the grid is $\Delta = 3.2 d_p$, which proved to be sufficient to capture the mesoscale structures in such gas–solid flow [6,11,14].

3. Budget analyses

3.1. Filtered momentum transport equation budget analysis

As mentioned in the Introduction, performing Euler–Euler simulations on a coarse computational grid only gives access to low-pass filtered quantities. The filtered version of the Euler–Euler model is recalled in Appendix B. Resolved and sub-grid quantities that appear in the right-hand side (RHS) of the filtered momentum equation

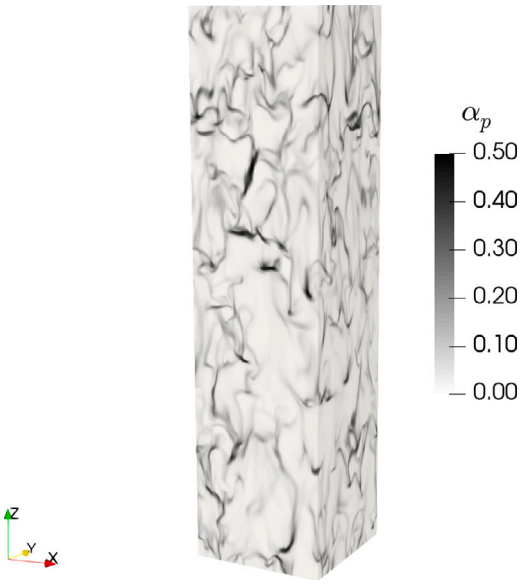

Fig. 1. Instantaneous particle volume fraction field α_p in a fine-grid Euler–Euler simulation of a tri-periodic fluidized bed of Geldart A particles, $\Delta = 3.2 d_p$.

(Eq. (B.6)) can be evaluated by applying an explicit filter onto the fine-grid data. In the present work, we use a box (or top-hat) filter $\bar{G}$ in the physical space:

$$\bar{G}(\mathbf{r}) = \begin{cases} 1/\bar{\Delta}^3, & |r_i| < 0.5\bar{\Delta},\ i = x, y, z \\ 0, & \text{otherwise,} \end{cases} \tag{1}$$

where $\bar{\Delta}$ is the filter width. The different terms in the RHS of Eq. (B.6) have been evaluated and then averaged over the whole domain. Fig. 2 shows the evolution of the resolved and sub-grid drag and pressure gradient terms in the vertical direction as the inverse of the Froude number based on the filter width ($Fr_{\bar{\Delta}}^{-1} = \frac{g\bar{\Delta}}{U_t^2}$) increases. All quantities have been normalized by the average gravitational term $\mathcal{W} = \{\alpha_p\}\rho_p g$, where the notation $\{.\}$ indicates the statistical average, here computed as a spatial average over the whole domain. The sub-grid pressure gradient term $\Phi_{p,z}^{sgs}$ (defined by Eq. (B.7)) appears to be negligible with respect to the drag and gravity terms, as previously reported for wall-bounded bubbling [14,34] and circulating [15] fluidized beds. However, other authors [40,41] claim that the sub-grid buoyancy contribution can be significant and should be modeled as an effective added mass contribution. On the contrary, the sub-grid drag force term $I_{p,z}^{sgs}$ increases significantly (in absolute value) with the size of the filter. As observed in many earlier studies [6,7,12,14,15], Fig. 2 indicates that the omission of the sub-grid contribution results in a drastic overestimation of the effective drag force. Owing to the periodicity of the three directions, the domain-averaged fluxes terms in the RHS of Eq. (B.6) cancel out exactly, although their sub-grid contributions has been verified to be locally negligible with respect to the gravity and drag force terms.

Besides, it has been widely demonstrated [14,15,42] that, in moderately dense gas–solid flows, the filtered drag force term $\langle \mathbf{I}_p \rangle$ can be approximated as

$$\langle \mathbf{I}_p \rangle \simeq \frac{\rho_p}{\tilde{\tau}_p} \langle \alpha_p (\mathbf{u}_g - \mathbf{u}_p) \rangle, \tag{2}$$

where $\tilde{\tau}_p$ is the resolved particle relaxation time computed from filtered quantities. Fig. 3 further confirms that the correlation between the left- and right-hand sides of Eq. (2) is very high in the vertical direction, with a coefficient of determination $R^2 = 0.984$. Therefore, the sub-grid drag force term can be written as

$$\mathbf{I}_p^{sgs} = \langle \mathbf{I}_p \rangle - \tilde{\mathbf{I}}_p$$

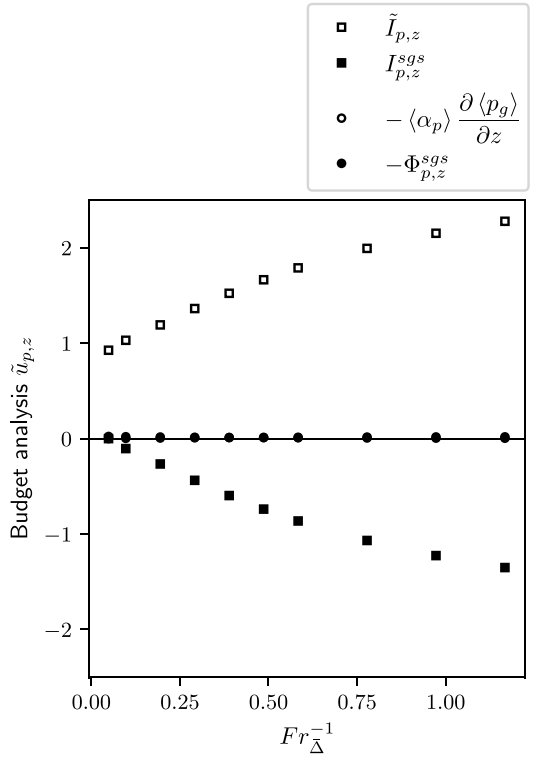

Fig. 2. Budget analysis of the filtered solid phase momentum transport equation (Eq. (B.6)) in the vertical direction (the resolved and sub-grid pressure gradient terms cannot be distinguished). All terms are averaged over the whole domain and normalized by $\mathcal{W} = \{\alpha_p\}\,\rho_p g$.

$$
\begin{aligned}
&\simeq \frac{\rho_p}{\tilde{\tau}_p}\left(\left\langle\alpha_p\left(\mathbf{u}_g-\mathbf{u}_p\right)\right\rangle-\left\langle\alpha_p\right\rangle\left(\tilde{\mathbf{u}}_g-\tilde{\mathbf{u}}_p\right)\right)\\
&=\frac{\rho_p}{\tilde{\tau}_p}\left(\left\langle\alpha_p\mathbf{u}_g\right\rangle-\left\langle\alpha_p\right\rangle\tilde{\mathbf{u}}_g\right)\\
&\triangleq\frac{\rho_p}{\tilde{\tau}_p}\left\langle\alpha_p\right\rangle\mathbf{v}_d,
\end{aligned}
\tag{3}
$$

where we introduced the drift velocity $\mathbf{v}_d$, defined as

$$
\mathbf{v}_d=\frac{\left\langle\alpha_p\mathbf{u}_g\right\rangle}{\left\langle\alpha_p\right\rangle}-\tilde{\mathbf{u}}_g. \tag{4}
$$

From Eq. (4), it comes that the drift velocity quantifies the difference between the mean velocity of the gas seen by the particles at the sub-grid scale and the resolved gas phase velocity. Hence, it is reasonable to consider that the closure of the sub-grid drag force term boils down to providing a model for the drift velocity.

3.2. Drift velocity transport equation budget analysis

In order to formulate a new physically grounded model for the drift velocity, we derive a transport equation for $\mathbf{v}_d$, as first suggested by Jiang et al. [38]. Starting from the 'microscale' Euler–Euler model given by Eqs. (A.1) and (A.2) and using the definition of the drift velocity (Eq. (4)), a transport equation is obtained:

$$
\frac{\partial}{\partial t}(\langle\alpha_p\rangle\,\rho_p v_{d,i})+\frac{\partial}{\partial x_j}(\langle\alpha_p\rangle\,\rho_p v_{d,i}\tilde{u}_{p,j})=\mathcal{P}^{sgs}_i+\mathcal{D}^{sgs}_i+\mathcal{\Psi}^{sgs}_i+\mathcal{A}^{sgs}_i+\mathcal{B}^{sgs}_i, \tag{5}
$$

where the different terms in the right-hand side are defined as

$$
\begin{aligned}
\mathcal{P}^{sgs}_i&=-\frac{\rho_p}{\rho_g}\left(1+\frac{\langle\alpha_p\rangle}{\langle\alpha_g\rangle}\right)\Phi^{sgs}_{p,i},\\
\mathcal{D}^{sgs}_i&=\left\langle\frac{\alpha_p\rho_p}{\alpha_g\rho_g}I_{g,i}\right\rangle-\frac{\langle\alpha_p\rangle\,\rho_p}{\langle\alpha_g\rangle\,\rho_g}\langle I_{g,i}\rangle,
\end{aligned}
$$

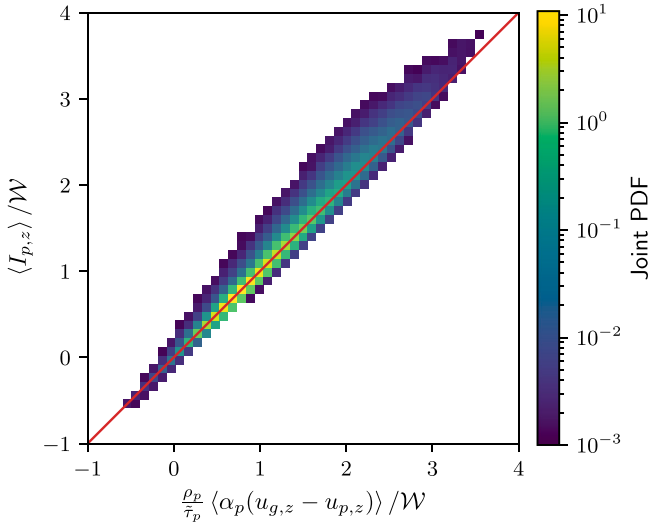

Fig. 3. Approximation of the filtered drag force term in the filtered momentum transport equation: correlation between the left- and right-hand sides of Eq. (2) in the vertical direction ($R^2 = 0.984$), $Fr^{-1}_{\tilde{\Delta}} = 0.486$.

$$
\begin{aligned}
\mathcal{\Psi}^{sgs}_i&=\left\langle\alpha_p\rho_p\left(u_{p,j}-u_{g,j}\right)\frac{\partial u_{g,i}}{\partial x_j}\right\rangle-\left\langle\alpha_p\right\rangle\rho_p\left(\tilde{u}_{p,j}-\tilde{u}_{g,j}\right)\frac{\partial\tilde{u}_{g,i}}{\partial x_j},\\
\mathcal{A}^{sgs}_i&=\frac{\left\langle\alpha_p\right\rangle\rho_p}{\left\langle\alpha_g\right\rangle\rho_g}\frac{\partial}{\partial x_j}\left(\left\langle\alpha_g\right\rangle\rho_g\sigma^{sgs}_{g,ij}\right),\\
\mathcal{B}^{sgs}_i&=-\frac{\partial}{\partial x_j}\left(\left\langle\alpha_p\right\rangle\rho_p\sigma^{sgs}_{pg,ij}\right),\\
\text{and }&\left\langle\alpha_p\right\rangle\rho_p\sigma^{sgs}_{pg,ij}\triangleq\left\langle\alpha_p\rho_p u_{g,i}u_{p,j}\right\rangle-\left\langle\alpha_p\right\rangle\rho_p\left(\tilde{u}_{g,i}+v_{d,i}\right)\tilde{u}_{p,j}.
\end{aligned}
$$

It must be noted that in Eq. (5) the drift velocity is transported by the resolved particle phase velocity $\tilde{\boldsymbol{u}}_p$, while in [38] the authors chose $\tilde{\boldsymbol{u}}_g$ as the transport velocity. In addition, the contribution of the filtered viscous stresses $\left\langle\boldsymbol{\Sigma}_g\right\rangle$ has been neglected in front of the other terms in the derivation of Eq. (5). Just as for the momentum transport equation, we examine the relative importance of the different terms appearing in the RHS of Eq. (5) when the size of the filter is increased. In a first approach, we focus on the vertical component of the drift velocity as it is expected to be the most crucial component to model. Fig. 4 indicates that the domain-averaged sub-grid terms related to the drag force, $\mathcal{D}^{sgs}_z$, and to the pressure gradient, $\mathcal{P}^{sgs}_z$, compensate each other. Other terms are exactly zero (owing to periodic conditions) or negligible. In addition, Fig. 5 shows that this equilibrium is also verified locally, which reads

$$
\left\langle\frac{\alpha_p\rho_p}{\alpha_g\rho_g}I_{g,z}\right\rangle-\frac{\left\langle\alpha_p\right\rangle\rho_p}{\left\langle\alpha_g\right\rangle\rho_g}\left\langle I_{g,z}\right\rangle-\frac{\rho_p}{\rho_g}\left(1+\frac{\left\langle\alpha_p\right\rangle}{\left\langle\alpha_g\right\rangle}\right)\Phi^{sgs}_{p,z}=0. \tag{6}
$$

The sub-grid pressure gradient term $\Phi^{sgs}_{p,z}$ is however unknown in coarse-grid simulations. De Wilde [40] proposed to model this term as a virtual added mass force, using the variance of the particle volume fraction and the resolved pressure gradient. The contribution of this term to the final form of the drift velocity model and the need to provide a closure for $\Phi^{sgs}_{p,z}$ is discussed in the next section.

4. Drift velocity model derivation

4.1. Drag term linearization

In order to build a model for the drift velocity, we first need to provide a closure for the first term in the LHS of Eq. (6). This term reads

$$
\left\langle\frac{\alpha_p}{\alpha_g}\frac{\rho_p}{\rho_g}I_{g,z}\right\rangle=\frac{\rho_p^2}{\rho_g}\left\langle\frac{\alpha_p^2}{\alpha_g\tau_p}(u_{p,z}-u_{g,z})\right\rangle. \tag{7}
$$

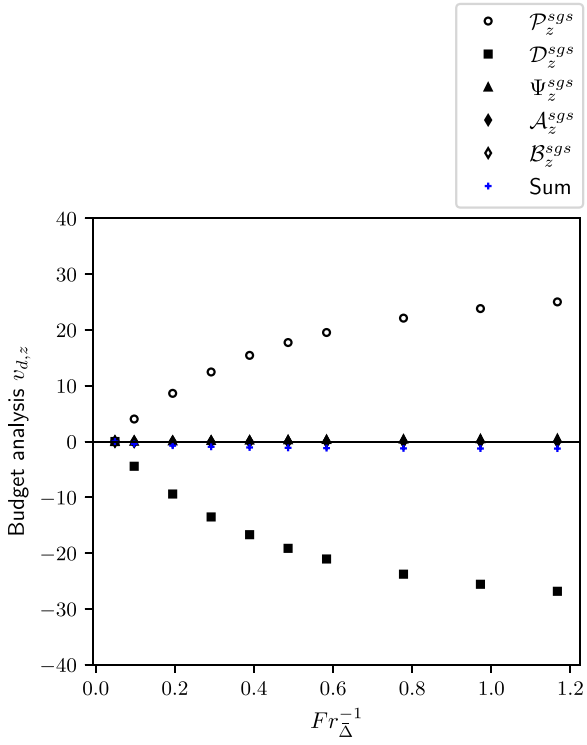

Fig. 4. Budget analysis of the drift velocity transport equation (Eq. (5)) in the vertical direction. All terms are averaged over the whole domain and normalized by $\mathcal{W} = \{\alpha_p\}\rho_p g$.

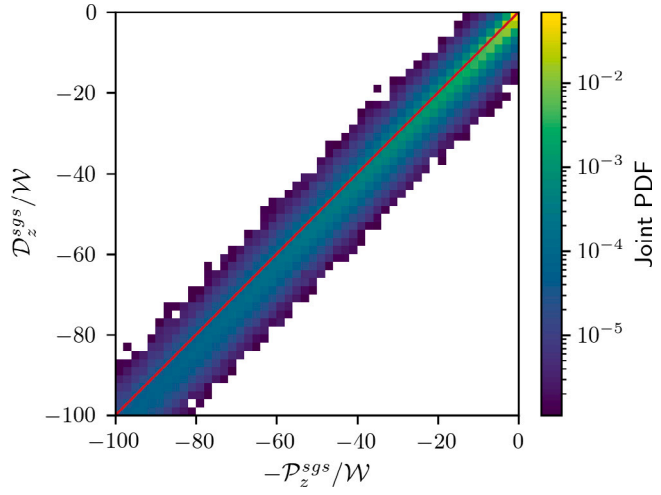

Fig. 5. Local equilibrium condition: correlation between the drag and pressure gradient terms in the transport equation of the drift velocity (Eq. (5)), $Fr_{\bar{\Delta}}^{-1} = 0.486$.

Similar to the treatment of the filtered drag force term in the momentum transport equation, it would be convenient to somehow linearize the RHS of Eq. (7) by taking the particle relaxation time τ_p out of the filtering operator. Fig. 6 shows that the approximation

$$\left\langle \frac{\alpha_p}{\alpha_g}\frac{\rho_p}{\rho_g} I_{g,z} \right\rangle \simeq \frac{\rho_p^2}{\rho_g \tilde{\tau}_p} \left\langle \frac{\alpha_p^2}{\alpha_g}(u_{p,z} - u_{g,z}) \right\rangle \tag{8}$$

is not as well verified as Eq. (2) (compare with Fig. 3). However, the coefficient of determination R^2 of this approximation is still fairly high ($R^2 = 0.910$) at $Fr_{\bar{\Delta}}^{-1} = 0.486$ (i.e. $\bar{\Delta} = 10\Delta$), so that we will assume it as valid for the rest of this work.

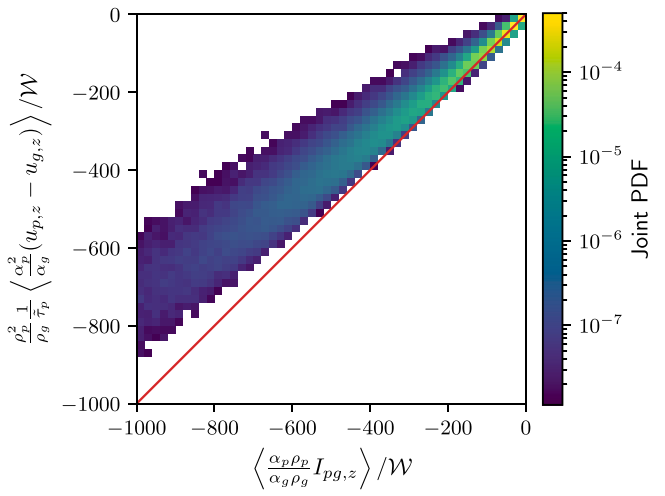

Fig. 6. Approximation of the filtered drag term in the drift velocity transport equation: correlation between the left- and right-hand side of Eq. (8) in the vertical direction ($R^2 = 0.910$), $Fr_{\bar{\Delta}}^{-1} = 0.486$.

From Eq. (3), it comes that the filtered drag force term $\langle I_{g,z} \rangle$ in the LHS of Eq. (6) can be expressed as

$$\langle I_{g,z} \rangle = \frac{\langle \alpha_p \rangle \rho_p}{\tilde{\tau}_p}(\tilde{u}_{p,z} - \tilde{u}_{g,z} - v_{d,z}). \tag{9}$$

Then, by introducing Eqs. (8) and (9) into the equilibrium condition given by Eq. (6), an analytical expression is obtained for the drift velocity:

$$v_{d,z} = \frac{\langle \alpha_g \rangle}{\langle \alpha_p \rangle^2}\left(\frac{\tilde{\tau}_p}{\rho_p}\left(1 + \frac{\langle \alpha_p \rangle}{\langle \alpha_g \rangle}\right)\Phi_{p,z}^{sgs} + \frac{\langle \alpha_p \rangle^2}{\langle \alpha_g \rangle}(\tilde{u}_{p,z} - \tilde{u}_{g,z}) - \left\langle \frac{\alpha_p^2}{\alpha_g}(u_{p,z} - u_{g,z}) \right\rangle \right). \tag{10}$$

With the sub-grid terms $\Phi_{p,z}^{sgs}$ and $\left\langle \frac{\alpha_p^2}{\alpha_g}(u_{p,z} - u_{g,z}) \right\rangle$ being evaluated from our fine-grid data, Fig. 7 shows that Eq. (10) provides a highly accurate model to estimate the drift velocity in the vertical direction ($R^2 = 0.966$). Next paragraph addresses the closure of the sub-grid correlation between the slip velocity and the ratio $\frac{\alpha_p^2}{\alpha_g}$.

4.2. Sub-grid correlations and large-eddy PDF approach

In order to close the terms $\left\langle \frac{\alpha_p^2}{\alpha_g}\mathbf{u}_p \right\rangle$ and $\left\langle \frac{\alpha_p^2}{\alpha_g}\mathbf{u}_g \right\rangle$ that appear in Eq. (10), we develop below a general approach to model the sub-grid correlations $\langle h(\alpha_p)\mathbf{u}_g \rangle$ and $\langle h(\alpha_p)\mathbf{u}_p \rangle$, where $h(\alpha_p)$ is some function of the local solid volume fraction. The former sub-grid correlation is formally defined as

$$\langle h(\alpha_p)\mathbf{u}_g \rangle (\mathbf{x}, t) = \int h(\alpha_p(\mathbf{y}, t))\mathbf{u}_g(\mathbf{y}, t)\bar{G}(\mathbf{y} - \mathbf{x})\, d\mathbf{y}. \tag{11}$$

Then, following the large-eddy PDF approach introduced by Gao et al. [43] for LES of turbulent reacting flows, Eq. (11) can be re-written as

$$\langle h(\alpha_p)\mathbf{u}_g \rangle (\mathbf{x}, t) = \iint h(A_p)\mathbf{U}_g f_{pg}^{sgs}(A_p, \mathbf{U}_g; \mathbf{x}, t)\, d\mathbf{U}_g dA_p, \tag{12}$$

where

$$f_{pg}^{sgs}(A_p, \mathbf{U}_g; \mathbf{x}, t) = \int \delta(A_p - \alpha_p(\mathbf{y}, t))\delta(\mathbf{U}_g - \mathbf{u}_g(\mathbf{y}, t))\bar{G}(\mathbf{y} - \mathbf{x})\, d\mathbf{y} \tag{13}$$

is the so-called large-eddy joint PDF, while A_p and $\mathbf{U}_g$ represent the phase space of α_p and $\mathbf{u}_g$, respectively. In Appendix C, we detail the

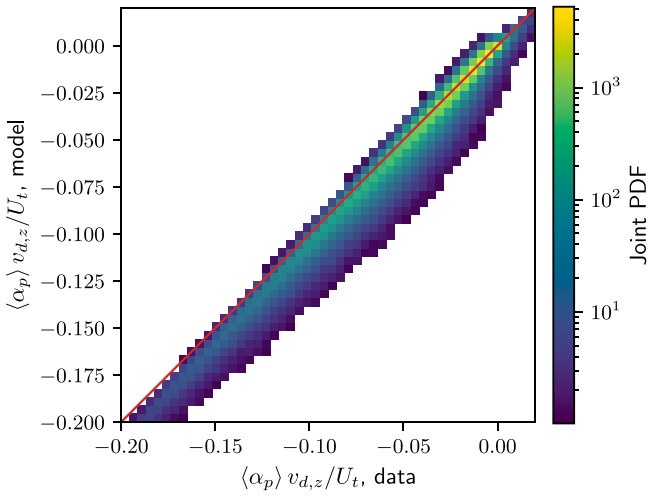

Fig. 7. Correlation between the drift velocity model given by Eq. (10) and the fine-grid data ($R^2 = 0.966$), $Fr_{\Delta}^{-1} = 0.486$.

different assumptions and mathematical developments that allow us to close the sub-grid correlations $\langle h(\alpha_p)\mathbf{u}_p\rangle$ and $\langle h(\alpha_p)\mathbf{u}_g\rangle$ on that basis. To sum up, we first show that the problem comes down to providing a model for the conditional average of the phase velocities ($\mathbf{u}_g$ and $\mathbf{u}_p$) as a function of a few filtered quantities. Second, we propose a simple linear model for these conditional averages. Doing so, the sub-grid correlations $\left\langle \frac{\alpha_p^2}{\alpha_g}\mathbf{u}_g \right\rangle$ and $\left\langle \frac{\alpha_p^2}{\alpha_g}\mathbf{u}_p \right\rangle$ that were left unclosed in Eq. (10) can be approximated by

$$\left\langle \frac{\alpha_p^2}{\alpha_g}\mathbf{u}_g \right\rangle = \left\langle \frac{\alpha_p^2}{\alpha_g} \right\rangle \tilde{\mathbf{u}}_g + \Gamma_g \mathbf{v}_d \tag{14}$$

and

$$\left\langle \frac{\alpha_p^2}{\alpha_g}\mathbf{u}_p \right\rangle = \left\langle \frac{\alpha_p^2}{\alpha_g} \right\rangle \tilde{\mathbf{u}}_g + \Gamma_p \mathbf{w}_d, \tag{15}$$

where the scalar coefficients Γ_g and Γ_p are given by

$$\Gamma_g \triangleq \left\langle \frac{\alpha_p^2}{\alpha_g} \right\rangle \langle\alpha_p\rangle - \frac{1}{\chi}\left(\left\langle \alpha_p^2 \right\rangle - \left\langle \frac{\alpha_p^2}{\alpha_g} \right\rangle \langle\alpha_g\rangle \right), \tag{16}$$

$$\Gamma_p \triangleq \left\langle \frac{\alpha_p^2}{\alpha_g} \right\rangle \langle\alpha_g\rangle + \frac{1}{\chi}\left(\left\langle \alpha_p^2 \right\rangle - \left\langle \frac{\alpha_p^2}{\alpha_g} \right\rangle \langle\alpha_g\rangle \right). \tag{17}$$

and

$$\mathbf{w}_d = \frac{\langle \alpha_g \mathbf{u}_p \rangle}{\langle \alpha_g \rangle} - \tilde{\mathbf{u}}_p \tag{18}$$

is the so-called reciprocal drift velocity. This quantity is not captured on coarse grids and an appropriate closure should be provided (see Section 4.3). In Eqs. (16) and (17), χ is the scaled sub-grid variance of the particle volume fraction (or scalar variance in short), defined as

$$\chi \triangleq \frac{\left\langle \alpha_p'^2 \right\rangle}{\langle\alpha_p\rangle\left(1 - \langle\alpha_p\rangle\right)}. \tag{19}$$

Obviously, $\left\langle \alpha_p'^2 \right\rangle$ also requires closure, as discussed later. Fig. 8 shows the correlation between the definitions of Γ_g and Γ_p given by Eqs. (16) and (17), respectively, and their values derived from the filtering of the fine-grid data using Eqs. (14) and (15), in the vertical direction. The model derived for Γ_g seems to yield better results than its counterpart for Γ_p, though the global trend is well captured in both cases.

4.3. Model formulation and dynamic procedure

Now that a model has been proposed for the sub-grid correlations $\left\langle \frac{\alpha_p^2}{\alpha_g}\mathbf{u}_g \right\rangle$ and $\left\langle \frac{\alpha_p^2}{\alpha_g}\mathbf{u}_p \right\rangle$, we can derive an explicit expression for $\mathbf{v}_d$. Inserting the closures given by Eqs. (14) and (15) into Eq. (10), the drift velocity model in the vertical direction reads

$$v_{d,z} = \frac{\overbrace{\left(\left\langle \frac{\alpha_p^2}{\alpha_g} \right\rangle - \frac{\langle\alpha_p\rangle^2}{\langle\alpha_g\rangle} \right)\left(\tilde{u}_{p,z} - \tilde{u}_{g,z}\right)}^{\text{I}} + \overbrace{\Gamma_p w_{d,z}}^{\text{II}} \overbrace{- \frac{\tilde{\tau}_p}{\rho_p}\left(1 + \frac{\langle\alpha_p\rangle}{\langle\alpha_g\rangle}\right)\Phi_{p,z}^{sgs}}^{\text{III}}}{\Gamma_g - \frac{\langle\alpha_p\rangle^2}{\langle\alpha_g\rangle}} \tag{20}$$

Fig. 9 shows that the model given by Eq. (20) is able to capture the vertical component of the drift velocity with very good accuracy ($R^2 = 0.948$) although we can observe a slight shift in the slope of the graph when compared to Fig. 7. This results somehow validates the approach proposed in Section 4.2 and further detailed in Appendix C. It also suggests that the approximate estimation of Γ_p from Eq. (17) has only a limited impact on the prediction of the drift velocity.

It must be emphasized that, so far, the exact values of the unknown sub-grid quantities $\left\langle \frac{\alpha_p^2}{\alpha_g} \right\rangle$, $\mathbf{w}_d$ and $\boldsymbol{\Phi}_p^{sgs}$ have been used for the *a priori* evaluation of the model. In Fig. 10, the three terms in the RHS of Eq. (20) have been averaged over the whole domain for increasing filter sizes. It comes out that the first two terms become very rapidly dominant while the contribution of the third term (linked to the sub-grid pressure gradient) can be safely discarded. The correlation between the data and the model (20) when term III is set to zero is shown in Fig. 11. Quite surprisingly, the performance of the model is even slightly improved at this filter width, with a coefficient of determination $R^2 = 0.967$.

Then, one still needs to provide a model for the reciprocal velocity $\mathbf{w}_d$. This is not an easy task since nothing indicates that the modeling of $\mathbf{w}_d$ is less demanding than the present procedure developed for $\mathbf{v}_d$. Nevertheless, Fig. 12 suggests that, in a first approach, we could consider a simpler proportional model between $\mathbf{w}_d$ and $\mathbf{v}_d$, of the form

$$\mathbf{w}_d = -C\mathbf{v}_d. \tag{21}$$

It also comes from the comparison between Figs. 12(a) and 12(b) that the value of the proportionality constant C changes little when the filter width is doubled. Indeed, we found that a proportionality coefficient $C = 0.5$ was appropriate for a large range of filter widths. Obviously, the value of C has been calibrated for this specific case and a more fundamental modeling of $\mathbf{w}_d$ might be needed in the future.

By neglecting the sub-grid pressure gradient term (i.e. term III) and using the simple linear model given by Eq. (21), Eq. (20) is re-written as

$$v_{d,z} = \frac{\left\langle \frac{\alpha_p^2}{\alpha_g} \right\rangle - \frac{\langle\alpha_p\rangle^2}{\langle\alpha_g\rangle}}{C\Gamma_p + \Gamma_g - \frac{\langle\alpha_p\rangle^2}{\langle\alpha_g\rangle}}\left(\tilde{u}_{p,z} - \tilde{u}_{g,z}\right). \tag{22}$$

A few comments must be made regarding the form of the model given by Eq. (22) (later referred to as the base model). First, it is interesting to note that we recover the co-linearity between the drift velocity and the resolved slip velocity, which was previously assumed in functional modeling approaches. Besides, if term III was not discarded from Eq. (20), an additional dependence on the filtered pressure gradient would appear in the model, as suggested by Jiang et al. [38], with a form very similar to the expression that these authors inferred from their neural network procedure (see Eq. (22) in [38]). Furthermore, the

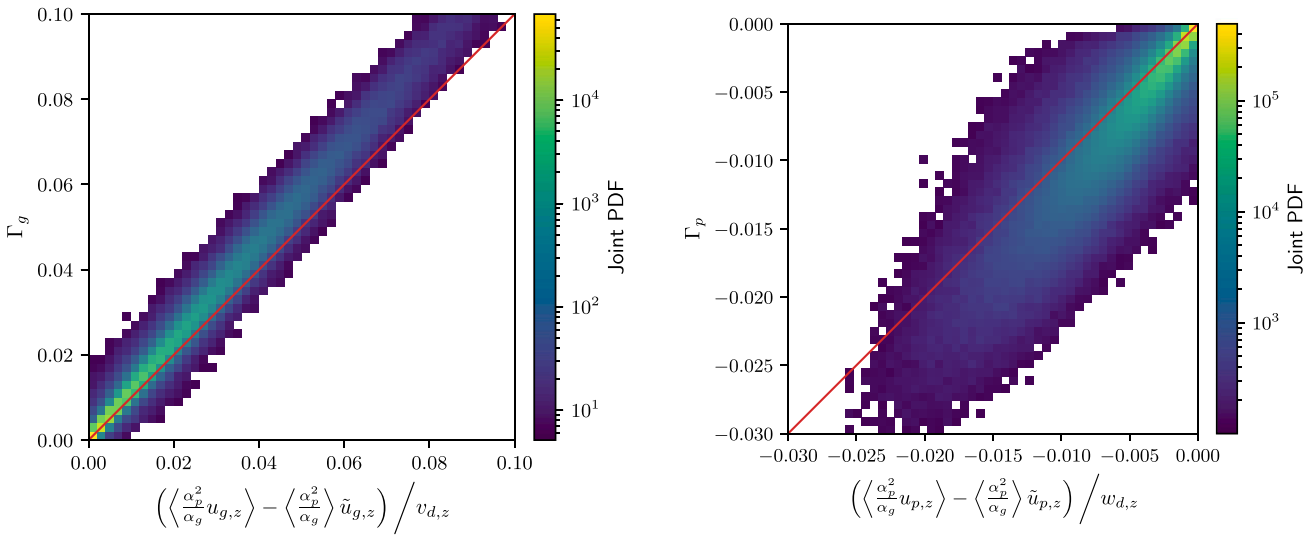

Fig. 8. Correlation between the estimation of Γ_g (left) and Γ_p (right) from Eqs. (16) and (17) and their evaluation from Eqs. (14) and (15), respectively. $Fr_{\bar{\Delta}}^{-1} = 0.486$.

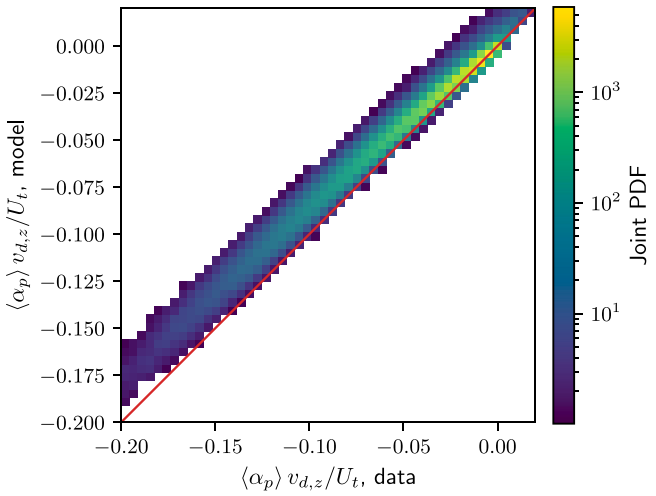

Fig. 9. Correlation between the drift velocity model given by Eq. (20) and the fine-grid data ($R^2 = 0.948$), $Fr_{\bar{\Delta}}^{-1} = 0.486$.

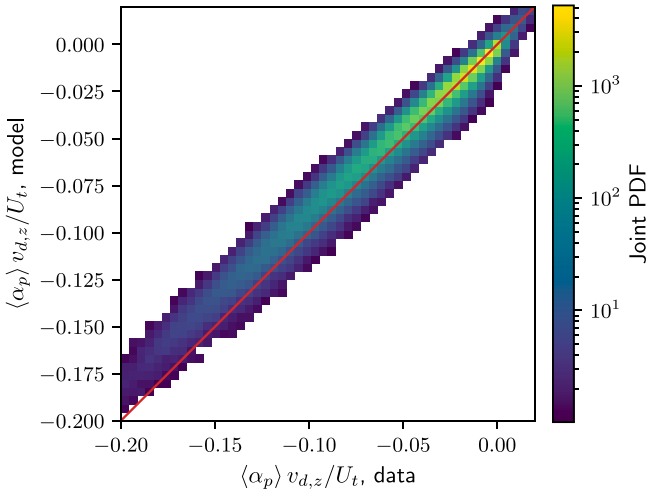

Fig. 11. Correlation between the drift velocity model given by Eq. (20) neglecting term III and the fine-grid data ($R^2 = 0.967$), $Fr_{\bar{\Delta}}^{-1} = 0.486$.

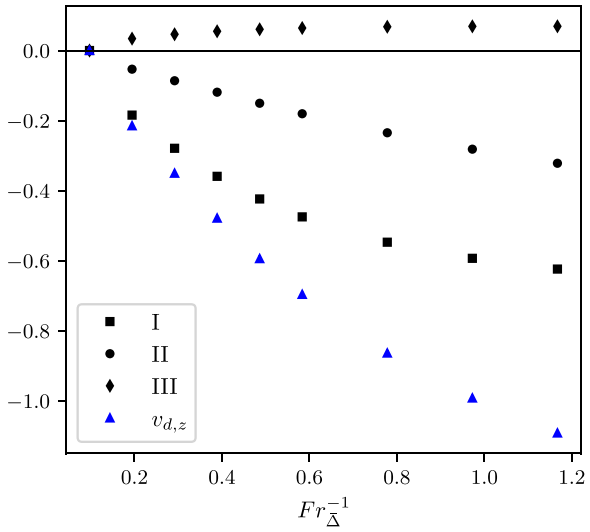

Fig. 10. Budget analysis of the drift velocity model given by Eq. (20). All terms have been averaged over the whole domain and normalized by the terminal velocity U_t.

model proposed by Eq. (22) does not depend explicitly on the filter size, unlike many previous studies [12,14,15], and therefore circumvents the issue to scale $\bar{\Delta}$ with the proper characteristic length scale in such flows (the reader is referred to [44,45] for a more detailed discussion on that topic).

Finally, it can be considered that the drift velocity model can be more generally written as

$$v_{d,z} = K_{zz} \frac{\left\langle \frac{\alpha_p^2}{\alpha_g} \right\rangle - \frac{\langle \alpha_p \rangle^2}{\langle \alpha_g \rangle}}{C\Gamma_p + \Gamma_g - \frac{\langle \alpha_p \rangle^2}{\langle \alpha_g \rangle}} \left(\tilde{u}_{p,z} - \tilde{u}_{g,z}\right)$$
$$\triangleq K_{zz} f\left(\langle \alpha_p \rangle, \left\langle \alpha_p'^2 \right\rangle, \left\langle \frac{\alpha_p^2}{\alpha_g} \right\rangle\right)(\tilde{u}_{p,z} - \tilde{u}_{g,z}), \tag{23}$$

where f is an algebraic function of a few filtered moments of α_p, and K_{zz} is the model constant that is dynamically adjusted using Germano's dynamic procedure [30], the details of which are provided in Appendix D. The performance of this dynamic model combined with the value given to the coefficient C is discussed in more detail below.

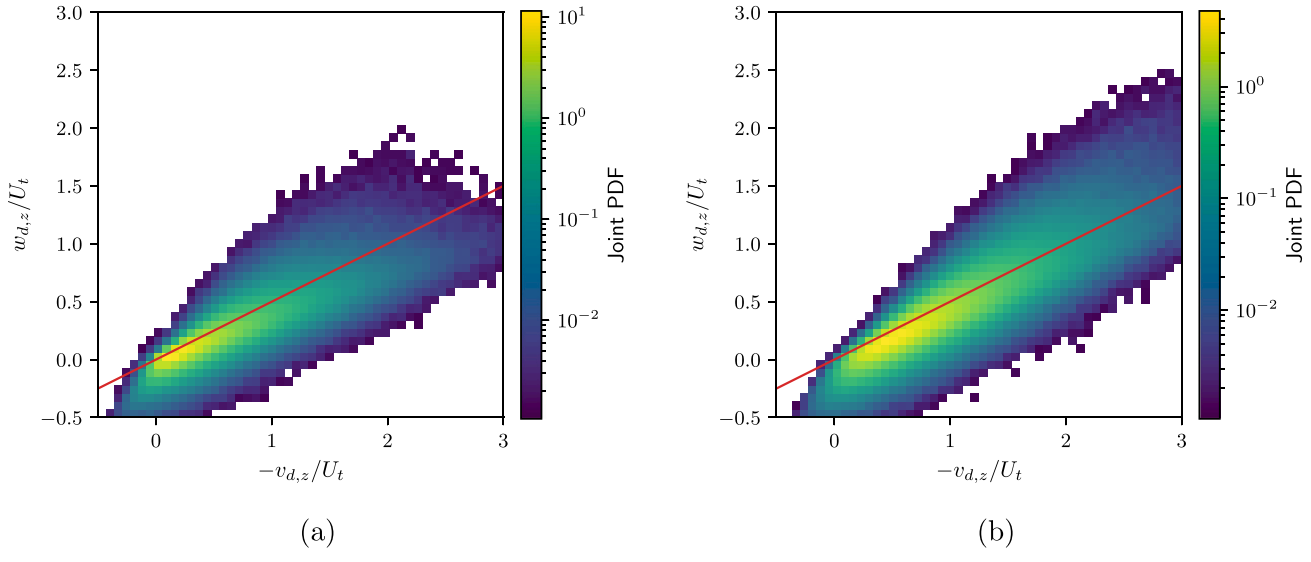

Fig. 12. Correlation between $w_{d,z}$ and $-v_{d,z}$ at (a) $Fr_{\tilde{\Delta}}^{-1} = 0.389$ and (b) $Fr_{\tilde{\Delta}}^{-1} = 0.778$. The solid red line corresponds to the slope $C = 0.5$.

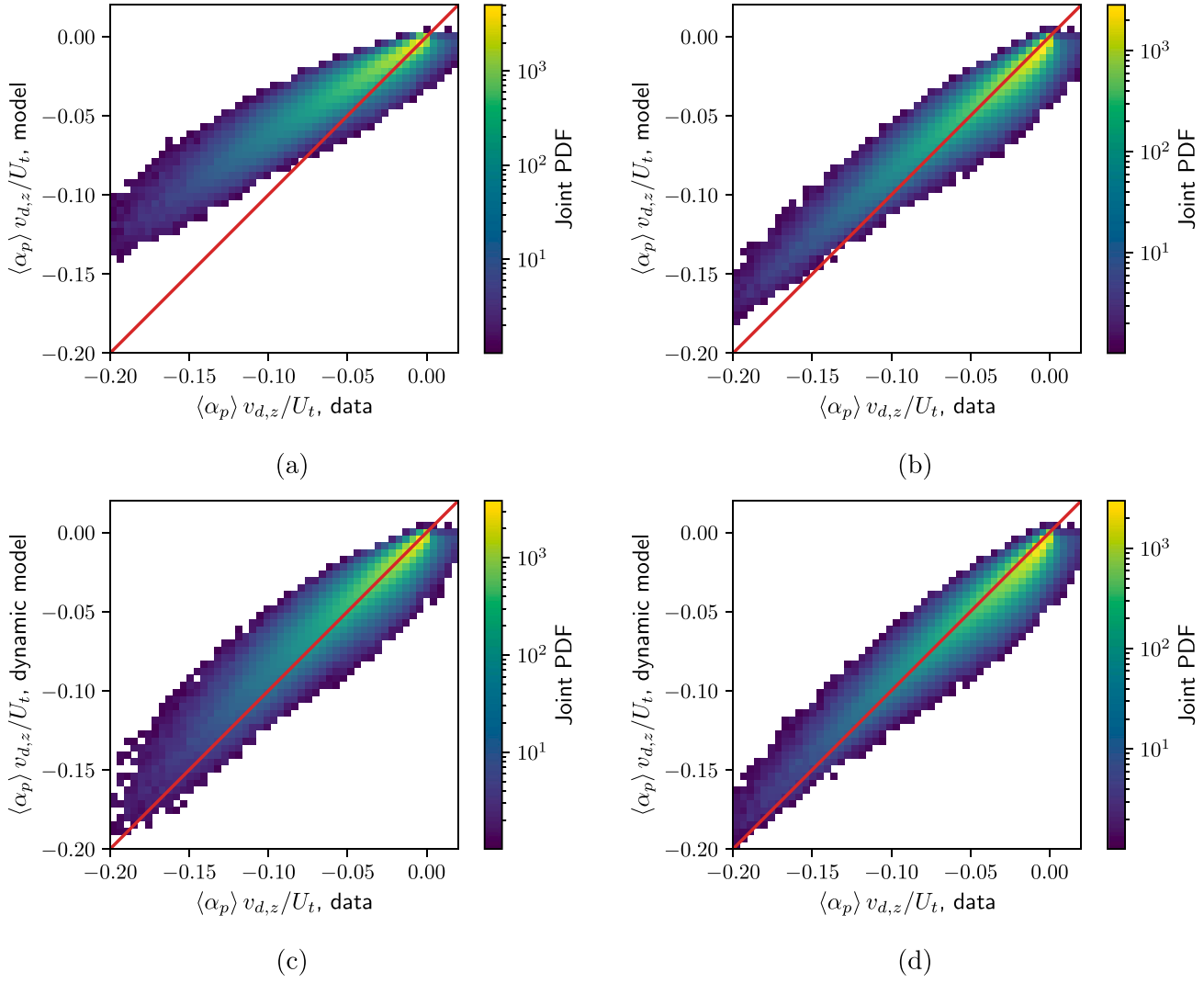

Fig. 13. Correlation between the drift velocity model given by Eq. (23) and the fine-grid data for Geldart A particles, $Fr_{\tilde{\Delta}}^{-1} = 0.486$. (a),(b): base model ($K_{zz} = 1$); (c),(d): dynamic adjustment of K_{zz}; (a),(c): $C = 0$; (b),(d): $C = 0.5$.

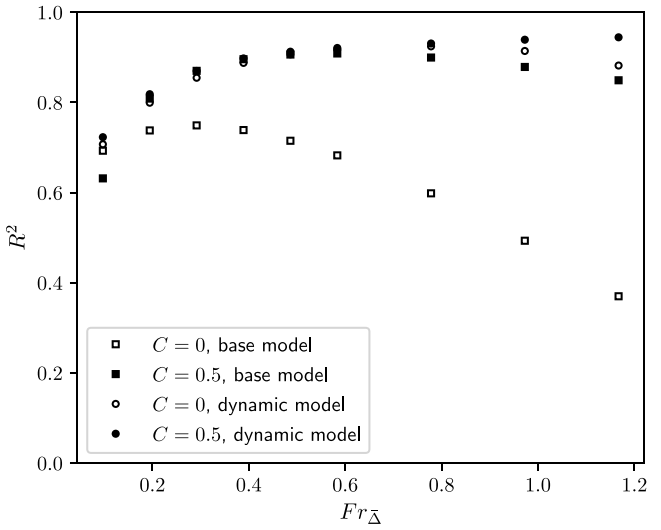

Fig. 14. Evolution of the coefficient of determination of the drift velocity model given by Eq. (23) with the filter size for Geldart A particles.

4.4. A priori model evaluation

The dynamic adjustment of the constant K_{zz} in Eq. (23) can be either implemented with $C = 0.5$ or by setting C to zero, which amounts to rely on the dynamic adjustment of K_{zz} to capture the full contribution of term II. Fig. 13 shows the correlation between the drift velocity computed from the fine-grid data and the model given by Eq. (23) with $K_{zz} = 1$, or using the dynamic adjustment, and with $C = 0$ or $C = 0.5$. It can be observed that, in the absence of dynamic procedure, neglecting the contribution of term II (i.e. $C = 0$) causes a significant shift in the slope of the correlation between the model and the data, while using the pre-estimated constant $C = 0.5$ decreases drastically the deviation from the unit slope. Besides, the dynamic procedure proves effective in correcting the slope of the base model, both for $C = 0$ and $C = 0.5$.

The coefficient of determination R^2 of the model given by Eq. (23) has been evaluated for the four cases discussed above and for a wide range of filter widths. It comes from Fig. 14 that when term II is neglected ($C = 0$) and that no dynamic procedure is implemented, the performance of the model decays very quickly as the filter size increases. The dynamic adjustment of K_{zz} leads to a major improvement in the performance of the model, although we still observe a slight decrease of R^2 for large filter widths. Interestingly, using the base model ($K_{zz} = 1$) with $C = 0.5$ yields almost identical performance. Finally, combining the dynamic procedure with the pre-estimated value $C = 0.5$ gives the best results, with a monotonic increase of R^2 with the filter width.

As a second validation step, the model has been tested in the case of Geldart B particles fluidization. The set-up is similar to that used for Geldart A particles and the simulation parameters for this case are summarized in Table 2. Fig. 15 indicates that neglecting term II also leads to a quick decay of the model performance as the filter width increases. Interestingly, using $C = 0.5$ in the model (23) yields very good results ($R^2 > 0.90$ for most filter widths) even though the model was developed and calibrated for Geldart A type particles. In this case, the dynamic procedure performs almost as well with $C = 0$ or $C = 0.5$. As a matter of fact, the former case is only outperformed by the latter for large filter widths. This result indicates that term II can be almost entirely accounted for through the dynamic procedure.

Finally, it must be pointed out that, so far, the exact values (i.e. computed from fine-grid data) of the filtered moments $\langle \alpha_p \rangle$, $\left\langle \alpha_p'^2 \right\rangle$ and $\left\langle \frac{\alpha_p^2}{\alpha_g} \right\rangle$ have been used for the derivation and evaluation of the drift velocity model. However, only the first of these three quantities is directly accessible in coarse-grid simulations. A functional closure relying only on the prior knowledge of the sub-grid variance is investigated in the next section.

Table 2
Physical and geometrical parameters used in fine-grid simulations of a tri-periodic fluidized bed of Geldart B particles.

Particle diameter d_p	150 μm
Particle density ρ_p	2500 kg/m^3
Average solid volume fraction $\{\alpha_p\}$	0.05
Restitution coefficient e_c	0.9
Gas density ρ_g	1.2 kg/m^3
Gas dynamic viscosity μ_g	1.8×10^{-5} Pa s
Terminal velocity U_t	0.988 m/s
Vertical dimension L_z	0.8372 m
Horizontal dimension $L_x = L_y$	0.2093 m
Grid size Δ	1308 μm
Fr_p	663.01
Fr_Δ	76.04

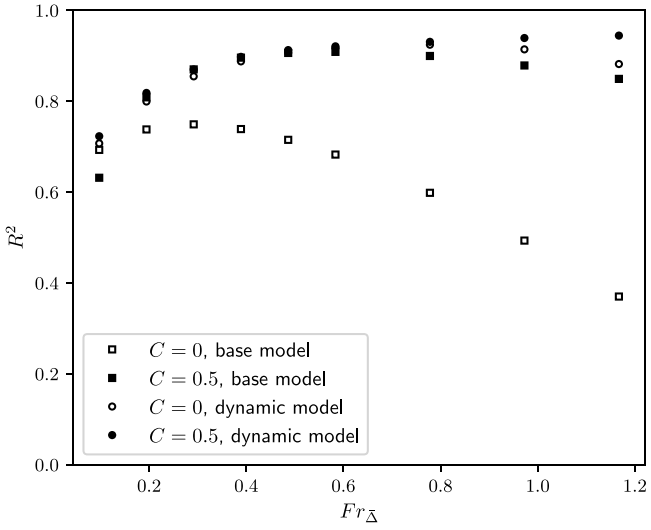

Fig. 15. Evolution of the coefficient of determination of the drift velocity model given by Eq. (23) with the filter size for Geldart B particles.

5. Functional drift velocity model

As mentioned earlier, the sub-grid moment $\left\langle \frac{\alpha_p^2}{\alpha_g} \right\rangle$ that shows up in the algebraic drift velocity model (23) remains unknown for a practical use in coarse-grid simulations. Still, we prospect that the function f in Eq. (23) can be fairly well approximated by a function of the first two filtered moments of the particle volume, i.e. the filtered value $\langle \alpha_p \rangle$ and the sub-grid variance $\left\langle \alpha_p'^2 \right\rangle$. If this is the case, one should be able to find a function f^* such that

$$f\left(\langle \alpha_p \rangle, \left\langle \alpha_p'^2 \right\rangle, \left\langle \frac{\alpha_p^2}{\alpha_g} \right\rangle\right) \simeq f^*(\langle \alpha_p \rangle, \chi) \tag{24}$$

where the scaled variance χ is defined in Eq. (19).

Fig. 16 shows the PDFs of $\langle \alpha_p \rangle$ and χ for different values of the filter width $\bar{\Delta}$ (the vertical axis in Fig. 16(b) has been intentionally cropped for readability reasons). The mean value of the distribution of $\langle \alpha_p \rangle$ remains constant and fixed by the domain-averaged particle volume fraction $\{\alpha_p\} = 0.05$, but the shape of the PDF in Fig. 16(a) tends towards a Dirac delta distribution as the filter size increases. On the other hand, the mean value of the normalized variance χ increases with $\bar{\Delta}$ since the level of heterogeneity at the sub-grid scale increases when coarser grids are used. It must be noted that the vast majority

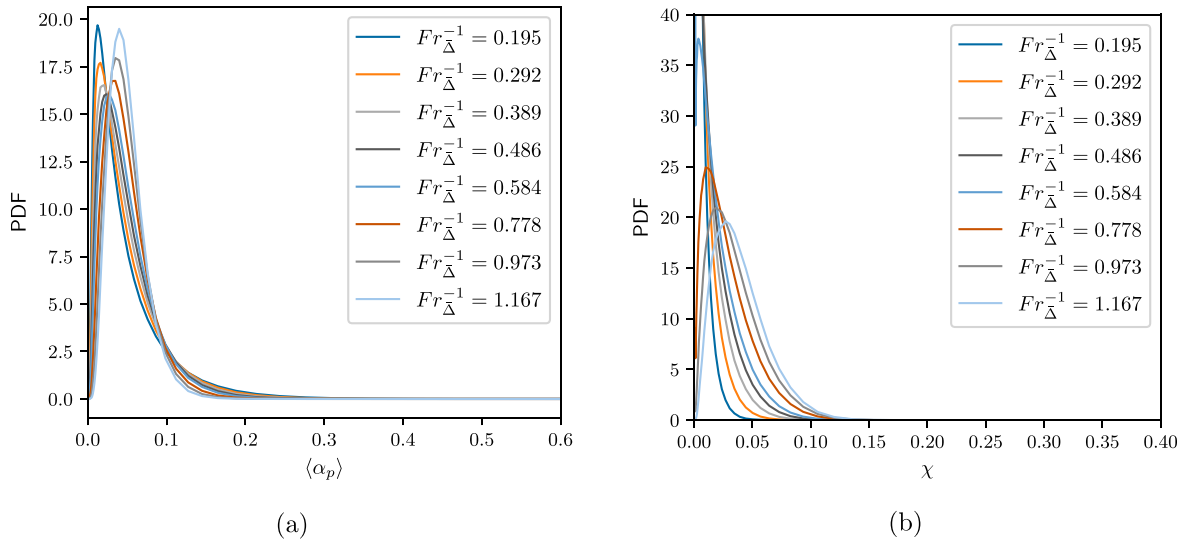

Fig. 16. Probability density functions of (a) $\langle \alpha_p \rangle$ and (b) χ for a range of filter widths.

of data are comprised in the intervals $\langle \alpha_p \rangle \in [0, 0.2]$ and $\chi \in [0, 0.15]$ whatever the filter width.

In a similar way to what has been proposed in previous studies [14, 15], the new bi-variate function f^* can be evaluated by conditional averaging over the whole domain as

$$f^*(\langle \alpha_p \rangle, \chi) = \frac{\{v_{d,z} | \langle \alpha_p \rangle, \chi\}}{\{(\tilde{u}_{p,z} - \tilde{u}_{g,z}) | \langle \alpha_p \rangle, \chi\}}. \tag{25}$$

To guarantee that the function $f^*(\langle \alpha_p \rangle, \chi)$ exists, one should prove that it is independent of the filter width. To do so, slices of the surface defined by the function $f^*(\langle \alpha_p \rangle, \chi)$ are taken at given values of $\langle \alpha_p \rangle$ and χ, for different filter widths $\bar{\Delta}$. Some of these slices are reported in Fig. 17 as well as their average over the different filters (solid black line). It turns out to be quite justified to assume that the function f^* is independent of the filter width, except at very low $\bar{\Delta}$, i.e. close to the fine-grid case. The case $Fr_{\bar{\Delta}}^{-1} = 0.097$ ($\bar{\Delta} = 2\Delta$) was therefore excluded from the averaging. Due to the scarcity of data, fluctuations about the mean curve look more important for large values of $\langle \alpha_p \rangle$ and χ. It can also be observed that the function f^* cancels out nicely when χ tends to zero. This is coherent with the absence of drag correction when the particles are homogeneously distributed at the sub-grid scale. Conversely, slices of f^* at given values of χ do not cancel when $\langle \alpha_p \rangle$ goes to zero. However, all data points at $\langle \alpha_p \rangle = 0$ merge at $\chi = 0$, by definition (see Eq. (19)). Therefore, in the absence of particles, no erroneous drag correction is applied.

In Fig. 18, we present the contours of the function f^* averaged over the different filter widths considered in this work, the smallest one excepted, as discussed above. It can be observed that, in the parameter space containing the vast majority of the data (roughly identified by $\langle \alpha_p \rangle \in [0, 0.2]$ and $\chi \in [0, 0.15]$) most of the variation of f^* is due to χ. This finding confirms that the drift velocity is intrinsically linked to the level of heterogeneity at the sub-grid scale. The dependence of the sub-grid drag force on the variance of the particle volume fraction has already been suggested in previous studies [34,35,37]. Ozel et al. [37] argued that the variance comes as an additional marker alongside the drift velocity, while here we consider that the drift velocity itself depends on the sub-grid variance. Schneiderbauer and co-workers [34,35] also proposed a drift velocity model depending on the sub-grid variance of α_p, but with an additional dependence on the sub-grid correlated kinetic energies of the gas and solid phases, requiring additional closures. Therefore, in the range of parameters identified by the red dashed box in Fig. 18, one could approximate the function f^* as a function of χ only,

$$f^*(\langle \alpha_p \rangle, \chi) \approx f_0^*(\chi). \tag{26}$$

Indeed, Fig. 19 confirms that cuts taken in the average 2-D function $f^*(\langle \alpha_p \rangle, \chi)$ at given values of $\langle \alpha_p \rangle$ in the range $[0, 0.2]$ collapse fairly well on a single curve. In addition, over the interval $\chi \in [0, 0.25]$, $f_0^*(\chi)$ was found to be nicely approximated by the following expression:

$$f_0^*(\chi) = \sqrt{\chi}(a_0 + a_1 \chi), \tag{27}$$

where $a_0 = 2.52$ and $a_1 = -2.87$. The drift velocity is then obtained as

$$v_{d,z} = f_0^*(\chi)(\tilde{u}_{p,z} - \tilde{u}_{g,z}). \tag{28}$$

As shown in Fig. 20, this simple functional model is able to capture the drift velocity very accurately over a large range of filter widths and for both Geldart A and Geldart B particles. Although the model was calibrated for Geldart A particles, the model performance is further improved in the case of Geldart B particles, without having to resort to a dynamic procedure, hence saving significant computational time.

However, the value of the sub-grid variance (and therefore of χ) remains unknown at the level of the coarse-grid. The modeling of the variance has namely been addressed by Schneiderbauer [34] who first derived a transport equation for $\left\langle \alpha_p'^2 \right\rangle$. Assuming local equilibrium, the author subsequently proposed an algebraic expression for $\left\langle \alpha_p'^2 \right\rangle$ which depends on the gradient of the filtered volume fraction, the gradient of the solid (or gas) phase filtered velocity and the solid (or gas) phase sub-grid kinetic energy. As mentioned earlier, this last sub-grid quantity must also be closed with an algebraic or a transport equation. Future works should therefore focus on two topics: (1) investigate new potential closures for $\left\langle \alpha_p'^2 \right\rangle$ and (2) evaluate the *a posteriori* performance of our drift velocity model when the sub-grid variance is known.

Finally, an alternative way of closing the drift velocity model proposed in Eq. (23) would be to provide an explicit closure for the sub-grid correlation $\left\langle \frac{\alpha_p^2}{\alpha_g} \right\rangle$. This approach is investigated in Appendix E for the interested reader. The proposed closure relies on a presumed sub-grid PDF for α_p which still requires the prior knowledge of the sub-grid variance. Though interesting from a theoretical perspective, we expect that the user of sub-grid models for coarse-grid simulations will be more inclined to use a functional expression of the form given by Eq. (28).

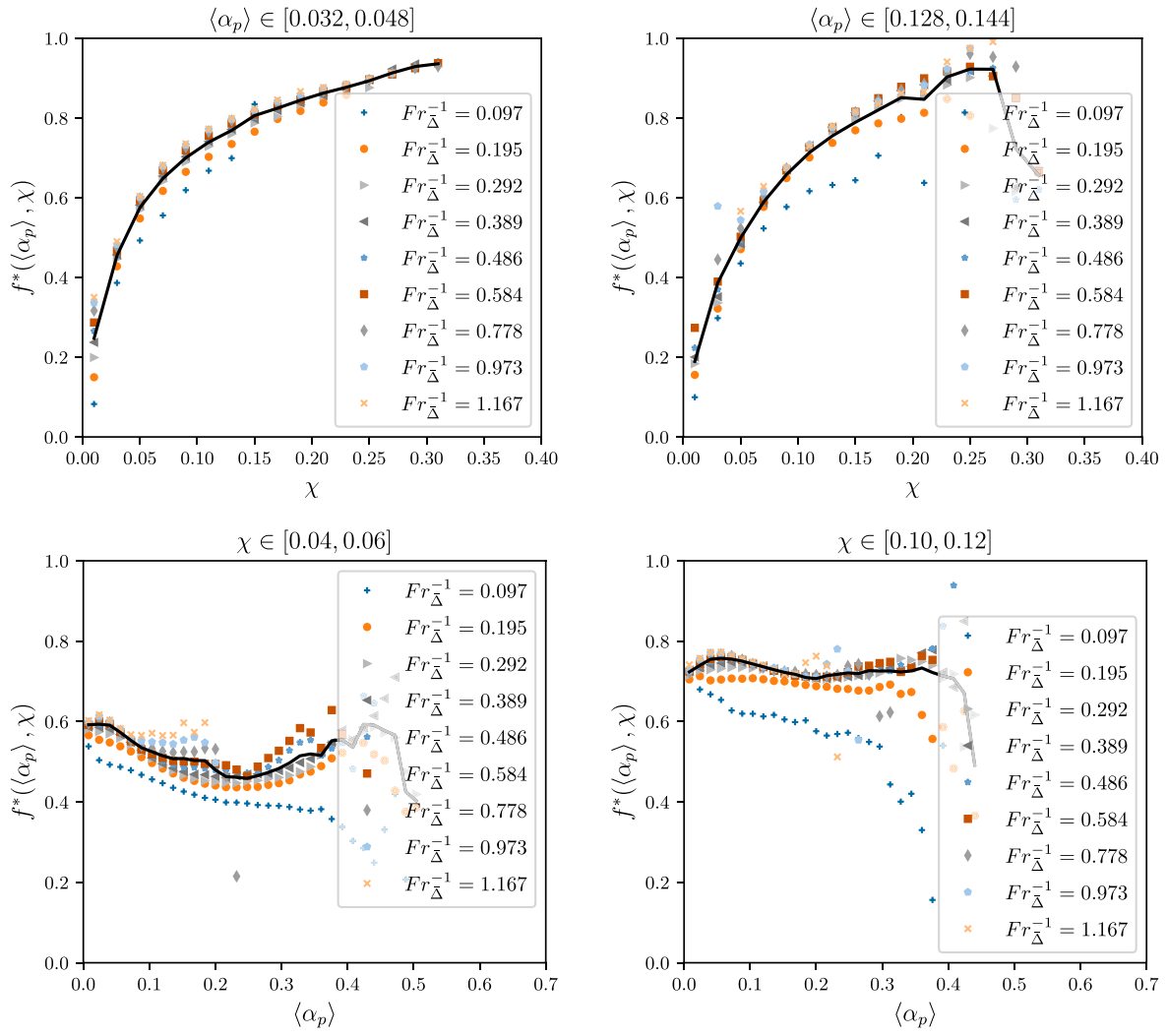

Fig. 17. 1-D cuts of the 2-D function $f^*(\langle\alpha_p\rangle, \chi)$ evaluated from conditional averaging (Eq. (25)) at given values of $\langle\alpha_p\rangle$ (top) and χ (bottom) and for different filter widths. The black solid line represents the average of function f^* over all filter widths except $Fr_{\bar{\Delta}}^{-1} = 0.097$.

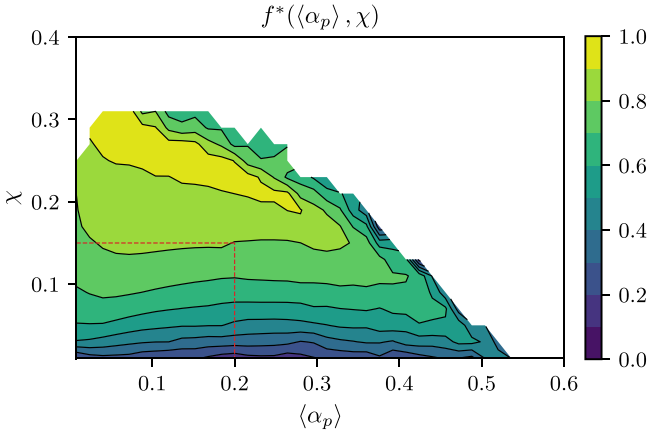

Fig. 18. Averaging of the model function $f^*(\langle\alpha_p\rangle, \chi)$ defined by Eq. (25) over the interval of filter widths defined by $Fr_{\bar{\Delta}} \in [0.195, 1.167]$.

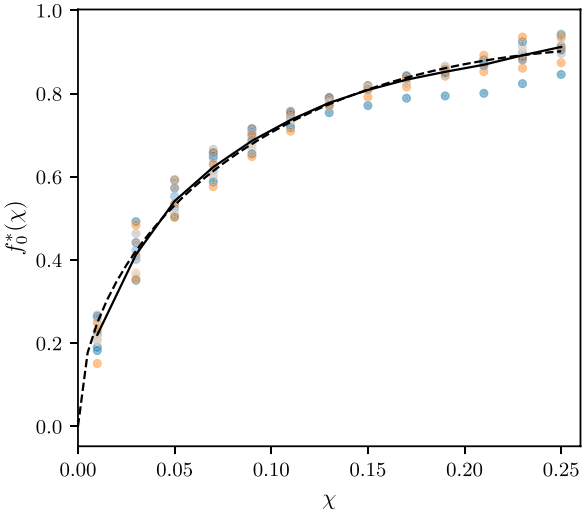

Fig. 19. Circles: 1-D cuts of the function $f^*(\langle\alpha_p\rangle, \chi)$ for different values of $\langle\alpha_p\rangle$ in the range $[0, 0.2]$. Solid line: average of 1-D cuts. Dashed line: approximation $f_0(\chi)$ given by Eq. (27).

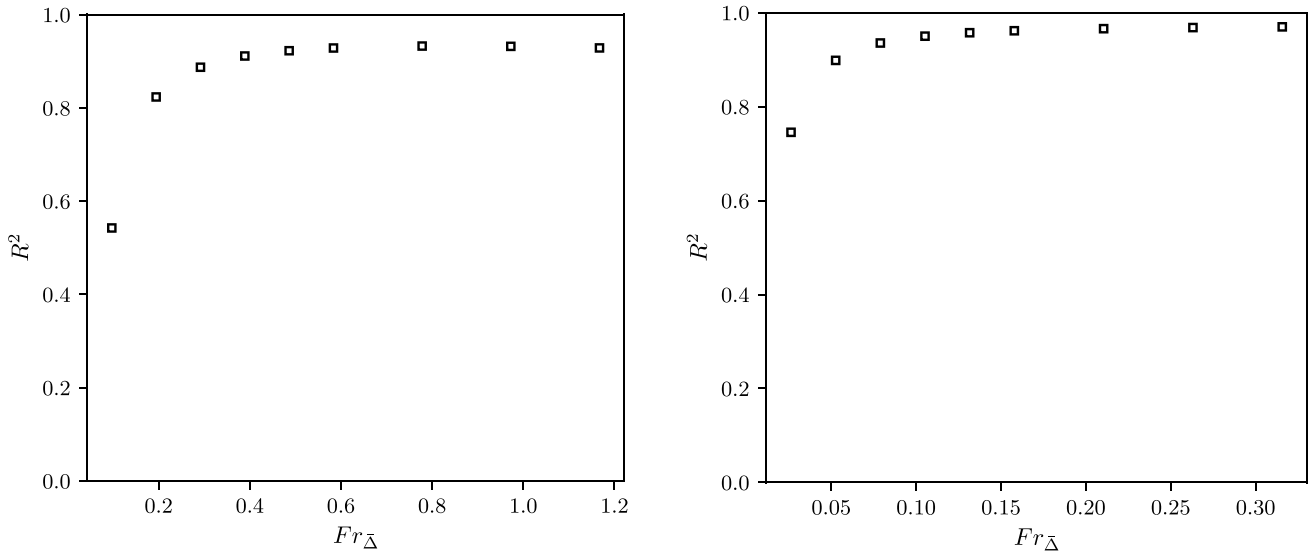

Fig. 20. Evolution of the coefficient of determination of the functional model given by Eq. (28) with the filter size for Geldart A (left) and Geldart B (right) particles.

6. Conclusion

The objective of this article was to derive a new physically grounded constitutive model for the sub-grid drag force term in the filtered Euler–Euler model. This term has been previously identified as the most crucial term to close in order to properly capture the hydrodynamics of gas–solid fluidized beds in coarse-grid simulations.

Following the works of Parmentier et al. and Ozel et al. [14,15], we first assert that the sub-grid drag force term can be found once the so-called drift velocity $\mathbf{v}_d$ is known. With this is mind, a transport equation has been derived for the drift velocity itself. The local equilibrium between the pressure- and drag-related terms in this transport equation was the starting point in order to derive a new algebraic model for the drift velocity.

Based on the large-eddy PDF approach proposed by Gao et al. [43] for LES of turbulent reacting flows, we derived an explicit algebraic model for the drift velocity (Eq. (20)) that still requires the knowledge of (i) sub-grid moments of α_p, (ii) the reciprocal drift velocity $\mathbf{w}_d$ and (iii) the sub-grid pressure gradient $\boldsymbol{\Phi}_p^{sgs}$. Eventually, the approximate model proposed in Eq. (23), coupled with a dynamic procedure, was shown to perform very well in *a priori* validation studies for both Geldart A and Geldart B particles ($R^2 > 0.90$). This model only involves filtered quantities and two sub-grid moments of the solid volume fraction $\left(\left\langle \alpha_p'^2 \right\rangle \text{ and } \left\langle \frac{\alpha_p^2}{\alpha_g} \right\rangle\right)$, avoiding explicit dependence on the filter size.

Then, it was shown that the function $f\left(\langle \alpha_p \rangle, \left\langle \alpha_p'^2 \right\rangle, \left\langle \frac{\alpha_p^2}{\alpha_g} \right\rangle\right)$ that appears in the new theoretical model could be captured, to a good approximation, by a uni-variate function of the form $f^*(\chi)$, where χ is the scaled sub-grid variance of the particle volume fraction. This function has been evaluated from our fine-grid data by conditional averaging over the whole domain, similar to previous studies [14,15]. The explicit model described by Eqs. (27) and (28) proved capable of predicting the drift velocity with very good accuracy, for both Geldart A and Geldart B particles and without resorting to a dynamic procedure.

Finally, it must be stressed once again that the approach developed in this study relies on the prior knowledge of the scalar variance, although $\left\langle \alpha_p'^2 \right\rangle$ is unknown at the level of a filtered cell. Future works should therefore investigate potential closures for $\left\langle \alpha_p'^2 \right\rangle$, namely by exploiting the scalar variance transport equation proposed by Schneiderbauer [34]. Once a reliable model is identified for $\left\langle \alpha_p'^2 \right\rangle$, the *a posteriori* performance of this new drift velocity model should be tested for different types of particles and fluidization regimes. We also intend to extend the present methodology to polydisperse flows, for which coarse-grid Eulerian simulations are still in their infancy.

CRediT authorship contribution statement

Baptiste Hardy: Conceptualization, Data curation, Formal analysis, Investigation, Methodology, Software, Visualization, Writing – original draft, Validation. **Pascal Fede:** Conceptualization, Funding acquisition, Methodology, Resources, Supervision, Writing – review & editing. **Olivier Simonin:** Conceptualization, Funding acquisition, Methodology, Resources, Supervision, Writing – review & editing.

Declaration of competing interest

The authors declare that they have no known competing financial interests or personal relationships that could have appeared to influence the work reported in this paper.

Data availability

Data will be made available on request.

Acknowledgments

The *netpune_cfd* software is a multiphase CFD solver developed in the framework of the NEPTUNE project financially supported by EDF (Electricité de France), CEA (Commissariat à l'Energie Atomique), France, IRSN (Institut de Radioprotection et de Sureté Nucléaire), France and Framatome, France.

This work was financially supported by the Carnot ISIFoR Institute, France under the REBIS project (2022/2023). It also benefited from HPC resources provided by the supercomputing centers CALMIP, France (project P0111) and GENCI, France (allocation A0142B06012).

Appendix A. Mathematical model

The numerical modeling is based on the Euler–Euler model where both the fluid and the solid phases are treated as inter-penetrating continua. We consider that the solid phase is made of spherical particles with constant diameter d_p.

The mass balance reads

$$\frac{\partial}{\partial t}\left(\alpha_k \rho_k\right) + \frac{\partial}{\partial x_j}\left(\alpha_k \rho_k u_{k,j}\right) = 0, \tag{A.1}$$

with α_k the volume fraction, ρ_k the density and u_k the local mean velocity of phase k (where $k = g$ for the gas and $k = p$ for the particles). Additionally, the particle and gas volume fractions must satisfy $\alpha_p + \alpha_g = 1$. The momentum transport equation for each phase is given by

$$\frac{\partial}{\partial t}\left(\alpha_k \rho_k u_{k,i}\right) + \frac{\partial}{\partial x_j}\left(\alpha_k \rho_k u_{k,i} u_{k,j}\right) = -\alpha_k \frac{\partial p_g}{\partial x_i} - \frac{\partial}{\partial x_j}\Sigma_{k,ij} + I_{k,i} + \alpha_k \rho_k g_i + \alpha_k F_i, \tag{A.2}$$

where p_g is the mean gas phase pressure, $\Sigma_{k,ij}$ is the stress tensor, $I_{k,i}$ is the interface momentum transfer term, g_i is the gravitational acceleration and F_i is the spatially uniform forcing term added to compensate for the weight of the mixture and computed as

$$F_i = -\frac{\sum_k m_k g_i}{V}, \tag{A.3}$$

where m_k is the total mass of phase k in the domain and V is the domain volume.

The momentum exchange term $I_{k,i}$ is modeled by considering only the drag force between the two phases (this assumption is fairly valid in gas–solid flows), i.e.

$$I_{p,i} = -I_{g,i} = \frac{\alpha_p \rho_p}{\tau_p}(u_{g,i} - u_{p,i}). \tag{A.4}$$

The particle relaxation time τ_p is evaluated from Wen and Yu drag law [46]:

$$\frac{1}{\tau_p} = \frac{1}{\tau_p^{St}}\left(1 + 0.15\mathrm{Re}_p^{0.685}\right)\alpha_g^{-2.7}, \tag{A.5}$$

with the particle Reynolds number $\mathrm{Re}_p = \frac{\alpha_g \rho_g \|\mathbf{v}_r\| d_p}{\mu_g}$, the relative (or slip) velocity $\mathbf{v}_r = \mathbf{u}_g - \mathbf{u}_p$ and the particle relaxation time in the Stokes flow limit $\tau_p^{St} = \frac{\rho_p d_p^2}{18\mu_g}$.

The gas phase stress tensor is given by

$$\Sigma_{g,ij} = -\mu_g\left(\frac{\partial u_{g,i}}{\partial x_j} + \frac{\partial u_{g,j}}{\partial x_i} - \frac{2}{3}\frac{\partial u_{g,m}}{\partial x_m}\delta_{ij}\right), \tag{A.6}$$

where μ_g is the gas dynamic viscosity, while the particulate stress tensor is defined as

$$\Sigma_{p,ij} = \left(p_p - \lambda_p \frac{\partial u_{p,m}}{\partial x_m}\right)\delta_{ij} - \mu_p\left(\frac{\partial u_{p,i}}{\partial x_j} + \frac{\partial u_{p,j}}{\partial x_i} - \frac{2}{3}\frac{\partial u_{p,m}}{\partial x_m}\delta_{ij}\right). \tag{A.7}$$

The particulate pressure, the bulk and shear viscosities (respectively p_p, λ_p and μ_p) are evaluated from the kinetic theory of granular flows:

$$p_p = \alpha_p \rho_p \left(1 + 2\alpha_p g_0 (1 + e_c)\right)\frac{2}{3}q_p^2$$

$$g_0 = \left(1 - \frac{\alpha_p}{\alpha_{p,max}}\right)^{-2.5\alpha_{p,max}}$$

$$\lambda_p = \frac{4}{3}\alpha_p^2 \rho_p d_p g_0 (1 + e_c)\sqrt{\frac{2}{3}\frac{q_p^2}{\pi}}$$

$$\mu_p = \alpha_p \rho_p (\nu_p^{kin} + \nu_p^{col})$$

$$\nu_p^{kin} = \frac{1}{2}\tau_p \frac{2}{3}q_p^2\left(1 + \alpha_p g_0 \boldsymbol{\Phi}_c\right) / \left(1 + \frac{\tau_p}{2}\frac{\sigma_c}{\tau_c}\right)$$

$$\nu_p^{col} = \frac{4}{5}\alpha_p g_0 (1 + e_c)\left(\nu_p^{kin} + d_p\sqrt{\frac{2}{3}\frac{q_p^2}{\pi}}\right),$$

where e_c is the collision restitution coefficient (comprised between 0 and 1) and $\alpha_{p,max} = 0.64$ is the particle volume fraction at maximum packing.

An additional transport equation is solved for the random kinetic energy of the particles q_p^2,

$$\frac{\partial}{\partial t}\left(\alpha_p \rho_p q_p^2\right) + \frac{\partial}{\partial x_j}\left(\alpha_p \rho_p q_p^2 u_{p,j}\right) = -\frac{\partial Q_j}{\partial x_j} + \Pi - \epsilon_c - \epsilon_v, \tag{A.8}$$

where:

$Q_j = -\alpha_p \rho_p \left(K_p^{kin} + K_p^{coll}\right)\frac{\partial q_p^2}{\partial x_j}$ is the diffusive term,

$\Pi = -\Sigma_{p,ij}\frac{\partial u_{p,i}}{\partial x_j}$ is the shear-induced production term,

$\epsilon_c = \frac{1}{3}(1 - e_c^2)\frac{\alpha_p \rho_p}{\tau_c} q_p^2$ is the dissipation term due to inelastic collisions,

$\epsilon_v = 2\frac{\alpha_p \rho_p}{\tau_p} q_p^2$ is the viscous dissipation term due to interaction of the particles with the gas phase.

The characteristic collision time scale τ_c, the kinetic diffusivity K_p^{kin} and the collisional diffusivity K_p^{coll} are respectively defined as

$$\tau_c = \frac{d_p}{24\alpha_p g_0}\sqrt{\frac{3\pi}{2q_p^2}}$$

$$K_p^{kin} = \frac{5}{9}\tau_p \frac{2}{3}q_p^2(1 + \alpha_p g_0 \phi_c) \Big/ \left(1 + \frac{5}{9}\tau_p \frac{\xi_c}{\tau_c}\right)$$

$$K_p^{coll} = \alpha_p g_0 (1 + e_c)\left(\frac{6}{5}K_p^{kin} + \frac{4}{3}d_p\sqrt{\frac{2}{3}\frac{q_p^2}{\pi}}\right),$$

and the model coefficients are

$$\phi_c = \frac{3}{5}(1 + e_c^2)(2e_c - 1)$$

$$\xi_c = \frac{1}{100}(1 + e_c)(49 - 33e_c)$$

$$\sigma_c = \frac{1}{5}(1 + e_c)(3 - e_c)$$

$$\boldsymbol{\Phi}_c = \frac{2}{5}(1 + e_c)(3e_c - 1).$$

Appendix B. Filtered Euler-Euler model

Given $\alpha_k(\mathbf{x}, t)$, the instantaneous volume fraction of phase k at a location $\mathbf{x}$ and time t, we can define the locally filtered volume fraction,

$$\langle \alpha_k(\mathbf{x}, t)\rangle = \int \alpha_k(\mathbf{y}, t)\bar{G}(\mathbf{y} - \mathbf{x}, t)d\mathbf{y}, \tag{B.1}$$

where $\bar{G}$ is the filtering operator satisfying $\int \bar{G}(\mathbf{r})df\mathbf{r} = 1$. We also define the phase average (or Favre average) of a quantity ψ over a phase k as

$$\langle \psi \rangle_k (\mathbf{x}, t) = \frac{1}{\langle \alpha_k \rangle}\int \alpha_k(\mathbf{y}, t)\psi(\mathbf{y}, t)\bar{G}(\mathbf{y} - \mathbf{x}, t)d\mathbf{y} = \frac{\langle \alpha_k \psi \rangle}{\langle \alpha_k \rangle} \tag{B.2}$$

Quantities resolved on the coarse LES grid will be noted with a superscript '~'. In particular, the phase-averaged velocities resolved on the coarse grid are written

$$\tilde{\mathbf{u}}_p = \frac{\langle \alpha_p \mathbf{u}_p \rangle}{\langle \alpha_p \rangle} = \langle \mathbf{u}_p \rangle_p, \tag{B.3}$$

$$\tilde{\mathbf{u}}_g = \frac{\langle \alpha_g \mathbf{u}_g \rangle}{\langle \alpha_g \rangle} = \langle \mathbf{u}_g \rangle_g. \tag{B.4}$$

Other quantities resolved on the coarse grid will follow the same notation, e.g. $\tilde{\tau}_p = \tau_p(\langle \alpha_p \rangle, \tilde{\mathbf{u}}_p, \tilde{\mathbf{u}}_g)$. The filtered mass and momentum transport equations are obtained by applying the filtering operator to Eqs. (A.1) and (A.2):

$$\frac{\partial}{\partial t}\left(\langle \alpha_k \rangle \rho_k\right) + \frac{\partial}{\partial x_j}\left(\langle \alpha_k \rangle \rho_k \tilde{u}_{k,j}\right) = 0, \tag{B.5}$$

$$\begin{aligned}\frac{\partial}{\partial t}\left(\langle \alpha_k \rangle \rho_k \tilde{u}_{k,i}\right) + \frac{\partial}{\partial x_j}\left(\langle \alpha_k \rangle \rho_k \tilde{u}_{k,i}\tilde{u}_{k,j}\right) = &-\langle \alpha_k \rangle \frac{\partial \langle p_g \rangle}{\partial x_i} - \boldsymbol{\Phi}_{k,i}^{sgs} \\ &- \frac{\partial}{\partial x_j}(\bar{\Sigma}_{k,ij} + \Sigma_{k,ij}^{sgs}) \\ &+ \tilde{I}_{k,i} + I_{k,i}^{sgs} - \frac{\partial}{\partial x_j}\left(\langle \alpha_k \rangle \rho_k \sigma_{k,ij}^{sgs}\right) \\ &+ \langle \alpha_k \rangle \rho_k g_i + \langle \alpha_k \rangle F_i.\end{aligned} \tag{B.6}$$

The sub-grid pressure gradient term $\Phi_{k,i}^{sgs}$ is defined as

$$\Phi_{k,i}^{sgs} = \left\langle \alpha_k \frac{\partial p_g}{\partial x_i} \right\rangle - \langle \alpha_k \rangle \frac{\partial \langle p_g \rangle}{\partial x_i} \tag{B.7}$$

and satisfies $\Phi_{p,i}^{sgs} = -\Phi_{g,i}^{sgs}$. The resolved and sub-grid interface momentum transfer terms are given by

$$\tilde{I}_{p,i} = \frac{\langle \alpha_p \rangle \rho_p}{\tilde{\tau}_p}(\tilde{u}_{g,i} - \tilde{u}_{p,i}) = -\tilde{I}_{g,i}, \tag{B.8}$$

and

$$I_{p,i}^{sgs} = \langle I_{p,i} \rangle - \tilde{I}_{p,i} = -I_{g,i}^{sgs}. \tag{B.9}$$

The sub-grid viscous stress tensor is given by

$$\Sigma_{k,ij}^{sgs} = \langle \Sigma_{k,ij} \rangle - \tilde{\Sigma}_{k,ij}, \tag{B.10}$$

and $\sigma_{k,ij}^{sgs}$ denotes the mesoscale (or 'Reynolds-like') stress tensor,

$$\sigma_{k,ij}^{sgs} = \langle u_{k,i} u_{k,j} \rangle_k - \tilde{u}_{k,i}\tilde{u}_{k,j}. \tag{B.11}$$

Appendix C. Derivation of the sub-grid correlations closures

We here detail the derivation of the closures proposed for the sub-grid correlations $\left\langle \frac{\alpha_p^2}{\alpha_g}\mathbf{u}_p \right\rangle$ and $\left\langle \frac{\alpha_p^2}{\alpha_g}\mathbf{u}_g \right\rangle$. As explained in Section 4.2, following the approach used by Gao et al. [43] for LES of turbulent reacting flows, Eq. (11) can be formally written as

$$\langle h(\alpha_p)\mathbf{u}_g \rangle (\mathbf{x}, t) = \iint h(A_p)\mathbf{U}_g f_{pg}^{sgs}(A_p, \mathbf{U}_g; \mathbf{x}, t)\, d\mathbf{U}_g dA_p. \tag{C.1}$$

For the sake of readability, we will keep in the following the notations α_p and $\mathbf{u}_g$ instead of A_p and $\mathbf{U}_g$, though it should be clear for the reader that this refers to a particular evaluation of α_p and $\mathbf{u}_g$ in their respective phase space.

First, it is assumed that the local large-eddy PDF defined by Eq. (13) can be approximated by the global joint PDF $f_{pg}(\alpha_p, \mathbf{u}_g)$, additionally conditioned by a few filtered quantities, namely;

$$f_{pg}^{sgs}(\alpha_p, \mathbf{u}_g; \mathbf{x}, t) \approx f_{pg}(\alpha_p, \mathbf{u}_g | \langle \alpha_p \rangle, \left\langle \alpha_p'^2 \right\rangle, \tilde{\mathbf{u}}_g, \mathbf{v}_d), \tag{C.2}$$

where the vertical bar '|' indicates the conditioning. In this study, the sub-grid variance of the solid volume fraction is defined as

$$\left\langle \alpha_p'^2 \right\rangle \triangleq \left\langle \alpha_p^2 \right\rangle - \langle \alpha_p \rangle^2, \tag{C.3}$$

although the identity $\langle \langle \alpha_p \rangle \rangle = \langle \alpha_p \rangle$ is not formally verified with LES filters such as the box or the Gaussian filter. Then, the joint PDF $f_{pg}(\alpha_p, \mathbf{u}_g | \langle \alpha_p \rangle, \left\langle \alpha_p'^2 \right\rangle, \tilde{\mathbf{u}}_g, \mathbf{v}_d)$ can also be expressed as the product of the marginal PDF of the gas phase velocity further conditioned by α_p and the PDF of the solid volume fraction $P(\alpha_p)$, i.e.

$$\begin{aligned} f_{pg}(\alpha_p, \mathbf{u}_g | \langle \alpha_p \rangle, \left\langle \alpha_p'^2 \right\rangle, \tilde{\mathbf{u}}_g, \mathbf{v}_d) &= f_g(\mathbf{u}_g | \alpha_p, \langle \alpha_p \rangle, \left\langle \alpha_p'^2 \right\rangle, \tilde{\mathbf{u}}_g, \mathbf{v}_d) \\ &\times P(\alpha_p | \langle \alpha_p \rangle, \left\langle \alpha_p'^2 \right\rangle, \tilde{\mathbf{u}}_g, \mathbf{v}_d). \end{aligned} \tag{C.4}$$

In the following, we will further assume that the PDF of α_p is independent of $\tilde{\mathbf{u}}_g$ and $\mathbf{v}_d$ when the two filtered quantities $\langle \alpha_p \rangle$ and $\left\langle \alpha_p'^2 \right\rangle$ are given, i.e.

$$P(\alpha_p | \langle \alpha_p \rangle, \left\langle \alpha_p'^2 \right\rangle, \tilde{\mathbf{u}}_g, \mathbf{v}_d) \approx P(\alpha_p | \langle \alpha_p \rangle, \left\langle \alpha_p'^2 \right\rangle). \tag{C.5}$$

Then, $\langle h(\alpha_p)\mathbf{u}_g \rangle$ can be expressed as

$$\begin{aligned} \langle h(\alpha_p)\mathbf{u}_g \rangle &= \int\int h(\alpha_p)\mathbf{u}_g f_g(\mathbf{u}_g | \alpha_p, \langle \alpha_p \rangle, \\ &\quad \left\langle \alpha_p'^2 \right\rangle, \tilde{\mathbf{u}}_g, \mathbf{v}_d) P(\alpha_p | \langle \alpha_p \rangle, \left\langle \alpha_p'^2 \right\rangle)\, d\mathbf{u}_g d\alpha_p \\ &= \int \left(h(\alpha_p) P(\alpha_p | \langle \alpha_p \rangle, \left\langle \alpha_p'^2 \right\rangle) \int \mathbf{u}_g f_g(\mathbf{u}_g | \alpha_p, \langle \alpha_p \rangle, \right. \\ &\quad \left. \left\langle \alpha_p'^2 \right\rangle, \tilde{\mathbf{u}}_g, \mathbf{v}_d) d\mathbf{u}_g \right) d\alpha_p \\ &= \int h(\alpha_p) P(\alpha_p | \langle \alpha_p \rangle, \left\langle \alpha_p'^2 \right\rangle) \left\{ \mathbf{u}_g | \alpha_p, \langle \alpha_p \rangle, \left\langle \alpha_p'^2 \right\rangle, \right. \\ &\quad \left. \tilde{\mathbf{u}}_g, \mathbf{v}_d \right\} d\alpha_p, \end{aligned} \tag{C.6}$$

where $\left\{ \mathbf{u}_g | \alpha_p, \langle \alpha_p \rangle, \left\langle \alpha_p'^2 \right\rangle, \tilde{\mathbf{u}}_g, \mathbf{v}_d \right\}$ is the statistical average of the gas phase velocity $\mathbf{u}_g$, conditioned by the local solid volume fraction and a number of filtered quantities. Hence, the equality (C.6) indicates that the sub-grid correlation $\langle h(\alpha_p)\mathbf{u}_g \rangle$ can be closed if we provide a model for the conditional average of the gas phase velocity. This result stems from the approximation made in Eq. (8), so that only the slip velocity appears inside the filtering operator.

By analogy, the sub-grid correlation involving the particle phase velocity is closed as

$$\begin{aligned} \langle h(\alpha_p)\mathbf{u}_p \rangle &= \int h(\alpha_p) P(\alpha_p | \langle \alpha_p \rangle, \left\langle \alpha_p'^2 \right\rangle) \left\{ \mathbf{u}_p | \alpha_p, \langle \alpha_p \rangle, \left\langle \alpha_p'^2 \right\rangle, \right. \\ &\quad \left. \tilde{\mathbf{u}}_p, \mathbf{w}_d \right\} d\alpha_p, \end{aligned} \tag{C.7}$$

where $\left\{ \mathbf{u}_p | \alpha_p, \langle \alpha_p \rangle, \left\langle \alpha_p'^2 \right\rangle, \tilde{\mathbf{u}}_p, \mathbf{w}_d \right\}$ is the conditional average of the solid phase velocity and $\mathbf{w}_d$ is the reciprocal drift velocity, defined as

$$\mathbf{w}_d = \frac{\langle \alpha_g \mathbf{u}_p \rangle}{\langle \alpha_g \rangle} - \tilde{\mathbf{u}}_p = \langle \mathbf{u}_p \rangle_g - \langle \mathbf{u}_p \rangle_p. \tag{C.8}$$

The analogy between the sub-grid joint PDF of α_p and $\mathbf{u}_g$ (or $\mathbf{u}_p$) and the corresponding global PDF conditioned by locally filtered quantities has shifted the closure problem to the modeling of the conditional average of the gas and solid phase velocities with respect to the local instantaneous particle volume fraction. For the gas phase, we propose a simple linear model of the form

$$\left\{ \mathbf{u}_g | \alpha_p, \langle \alpha_p \rangle, \left\langle \alpha_p'^2 \right\rangle, \tilde{\mathbf{u}}_g, \mathbf{v}_d \right\} = \mathbf{A}_g + \mathbf{B}_g(\alpha_p - \langle \alpha_p \rangle), \tag{C.9}$$

where $\mathbf{A}_g$ and $\mathbf{B}_g$ are functions of locally filtered quantities. This model must satisfy the known sub-grid moments between α_p and $\mathbf{u}_g$, namely,

$$\begin{aligned} \langle \alpha_g \mathbf{u}_g \rangle &= \int (1 - \alpha_p)\, P(\alpha_p | \langle \alpha_p \rangle, \left\langle \alpha_p'^2 \right\rangle) \left\{ \mathbf{u}_g | \alpha_p; \langle \alpha_p \rangle, \left\langle \alpha_p'^2 \right\rangle, \tilde{\mathbf{u}}_g, \mathbf{v}_d \right\} d\alpha_p \\ &= \langle \alpha_g \rangle \tilde{\mathbf{u}}_g, \end{aligned} \tag{C.10}$$

and

$$\begin{aligned} \langle \alpha_p \mathbf{u}_g \rangle &= \int \alpha_p\, P(\alpha_p | \langle \alpha_p \rangle, \left\langle \alpha_p'^2 \right\rangle) \left\{ \mathbf{u}_g | \alpha_p, \langle \alpha_p \rangle, \left\langle \alpha_p'^2 \right\rangle, \tilde{\mathbf{u}}_g, \mathbf{v}_d \right\} d\alpha_p \\ &= \langle \alpha_p \rangle (\tilde{\mathbf{u}}_g + \mathbf{v}_d). \end{aligned} \tag{C.11}$$

By introducing the general form of the conditional average gas phase velocity given by Eq. (C.9) into Eqs. (C.10) and (C.11), it comes that $\mathbf{A}_g$ and $\mathbf{B}_g$ are given by

$$\mathbf{A}_g = \tilde{\mathbf{u}}_g + \langle \alpha_p \rangle \mathbf{v}_d \tag{C.12}$$

and

$$\mathbf{B}_g = \frac{\mathbf{v}_d}{\chi}, \tag{C.13}$$

where χ is the scaled variance of the particle volume fraction, defined as

$$\chi \triangleq \frac{\left\langle \alpha_p'^2 \right\rangle}{\langle \alpha_p \rangle (1 - \langle \alpha_p \rangle)}. \tag{C.14}$$

Eventually, the conditional average gas velocity model reads

$$\left\{ \mathbf{u}_g | \alpha_p, \langle \alpha_p \rangle, \left\langle \alpha_p'^2 \right\rangle, \tilde{\mathbf{u}}_g, \mathbf{v}_d \right\} = \tilde{\mathbf{u}}_g + \mathbf{v}_d \left(\langle \alpha_p \rangle + \frac{1}{\chi}(\alpha_p - \langle \alpha_p \rangle) \right). \tag{C.15}$$

The methodology can be reproduced for the conditional average solid phase velocity, for which the following form is proposed:

$$\left\{ \mathbf{u}_p | \alpha_p, \langle \alpha_p \rangle, \left\langle \alpha_p'^2 \right\rangle, \tilde{\mathbf{u}}_p, \mathbf{w}_d \right\} = \mathbf{A}_p + \mathbf{B}_p(\alpha_p - \langle \alpha_p \rangle). \tag{C.16}$$

By using the identities

$$\langle \alpha_p \mathbf{u}_p \rangle = \langle \alpha_p \rangle \tilde{\mathbf{u}}_p \tag{C.17}$$

and

$$\left\langle \alpha_g \mathbf{u}_p \right\rangle = \left\langle \alpha_g \right\rangle (\tilde{\mathbf{u}}_p + \mathbf{w}_d), \tag{C.18}$$

it follows that $\mathbf{A}_p$ and $\mathbf{B}_p$ are given by

$$\mathbf{A}_p = \tilde{\mathbf{u}}_p + \left\langle \alpha_g \right\rangle \mathbf{w}_d \tag{C.19}$$

and

$$\mathbf{B}_p = -\frac{\mathbf{w}_d}{\chi}. \tag{C.20}$$

Hence, the model for the conditional average solid phase velocity reads

$$\left\{ \mathbf{u}_p | \alpha_p, \left\langle \alpha_p \right\rangle, \left\langle \alpha_p'^2 \right\rangle, \tilde{\mathbf{u}}_p, \mathbf{w}_d \right\} = \tilde{\mathbf{u}}_p + \mathbf{w}_d \left(\left\langle \alpha_g \right\rangle - \frac{1}{\chi} \left(\alpha_p - \left\langle \alpha_p \right\rangle \right) \right). \tag{C.21}$$

Introducing the expressions for the conditional averages given by Eqs. (C.15) and (C.21) into Eqs. (C.6) and (C.7), respectively, and by relying again on the equivalence between conditionally averaged quantities and their locally filtered counterpart, it comes that the sub-grid correlations $\left\langle \frac{\alpha_p^2}{\alpha_g} \mathbf{u}_g \right\rangle$ and $\left\langle \frac{\alpha_p^2}{\alpha_g} \mathbf{u}_p \right\rangle$ that were left unclosed in Eq. (10) can be expressed as

$$\left\langle \frac{\alpha_p^2}{\alpha_g} \mathbf{u}_g \right\rangle = \left\langle \frac{\alpha_p^2}{\alpha_g} \right\rangle \tilde{\mathbf{u}}_g + \Gamma_g \mathbf{v}_d \tag{C.22}$$

and

$$\left\langle \frac{\alpha_p^2}{\alpha_g} \mathbf{u}_p \right\rangle = \left\langle \frac{\alpha_p^2}{\alpha_g} \right\rangle \tilde{\mathbf{u}}_g + \Gamma_p \mathbf{w}_d, \tag{C.23}$$

where Γ_g and Γ_p are given by Eqs. (16) and (17), respectively.

Appendix D. Dynamic procedure

The model proposed in Eq. (23) for the vertical component of the drift velocity reads

$$v_{d,z} = K_{zz} f \left(\left\langle \alpha_p \right\rangle, \left\langle \alpha_p'^2 \right\rangle, \left\langle \frac{\alpha_p^2}{\alpha_g} \right\rangle \right) (\tilde{u}_{p,z} - \tilde{u}_{g,z}) \tag{D.1}$$

where the constant K_{zz} can be automatically adjusted via the dynamic procedure introduced by Germano [30], and more recently applied to multiphase turbulence [14,15,35]. The dynamic procedure relies on the hypothesis of turbulence scale similarity in the inertial range and on the use of a test filter with a larger filtering window than the implicit LES filter. Quantities computed at the test filter level should be accessible in practical coarse-grid simulations. The test filter is denoted '$\hat{}$' in the following.

The sub-grid scale drift velocity term at the test filter level is given by

$$\mathcal{T}_z = \widehat{\left\langle \alpha_p (u_{g,z} - u_{p,z}) \right\rangle} - \widehat{\left\langle \alpha_p \right\rangle} (\hat{\tilde{u}}_{g,z} - \hat{\tilde{u}}_{p,z}), \tag{D.2}$$

while the filtered sub-grid drift velocity term is

$$\hat{\tau}_z \triangleq \widehat{\left\langle \alpha_p \right\rangle v_{d,z}} = \widehat{\left\langle \alpha_p (u_{g,z} - u_{p,z}) \right\rangle} - \widehat{\left\langle \alpha_p \right\rangle (\tilde{u}_{g,z} - \tilde{u}_{p,z})}. \tag{D.3}$$

The difference between Eqs. (D.2) and (D.3) gives

$$\mathcal{L}_z = \mathcal{T}_z - \hat{\tau}_z = \left\langle \alpha_p \right\rangle \widehat{(\tilde{u}_{g,z} - \tilde{u}_{p,z})} - \widehat{\left\langle \alpha_p \right\rangle} (\hat{\tilde{u}}_{g,z} - \hat{\tilde{u}}_{p,z}), \tag{D.4}$$

which only involves filtered quantities available at the coarse-grid level. Then, using Eq. (D.1) to model the sub-grid drift velocity term and assuming that the constant K_{zz} is invariant between the scales, we have that

$$\mathcal{L}_z \simeq K_{zz} \mathcal{M}_z \tag{D.5}$$

where

$$\mathcal{M}_z = f \left(\widehat{\left\langle \alpha_p \right\rangle}, \widehat{\left\langle \alpha_p'^2 \right\rangle}, \widehat{\left\langle \frac{\alpha_p^2}{\alpha_g} \right\rangle} \right) \widehat{\left\langle \alpha_p \right\rangle} (\hat{\tilde{u}}_{p,z} - \hat{\tilde{u}}_{g,z}) - f \left(\left\langle \alpha_p \right\rangle, \left\langle \alpha_p'^2 \right\rangle, \widehat{\left\langle \frac{\alpha_p^2}{\alpha_g} \right\rangle} \right) \widehat{\left\langle \alpha_p \right\rangle} (\tilde{u}_{p,z} - \tilde{u}_{g,z}) \tag{D.6}$$

Finally, following Lilly [47], the spatially uniform model constant K_{zz} is best evaluated by averaging over the whole domain as

$$K_{zz} = \frac{\{ \mathcal{L}_z \mathcal{M}_z \}}{\{ \mathcal{M}_z \mathcal{M}_z \}}. \tag{D.7}$$

The explicit filter used in the physical space to estimate coarse-grid quantities is the top-hat filter $\bar{G}$ defined by Eq. (1), with a width $\bar{\Delta}$. In 1-D, the spectrum of this filter in the wavenumber space is given by

$$\bar{\mathcal{G}}(k) = \frac{\sin(k\bar{\Delta}/2)}{k\bar{\Delta}/2}. \tag{D.8}$$

When using the dynamic procedure, one generally requires that the global filter $\hat{\bar{G}}$ resulting from the successive application of the test and LES filters has twice the size of the LES filter, i.e. $\hat{\bar{\Delta}} = 2\bar{\Delta}$. To make it so, the spectrum of $\hat{\bar{G}}$ must be given by

$$\hat{\bar{\mathcal{G}}}(k) = \frac{\sin(k\bar{\Delta})}{k\bar{\Delta}}. \tag{D.9}$$

Since quantities evaluated at the test filter level are the result of the application of the test filter onto the coarse-grid quantities, the spectrum of the test filter to apply is

$$\hat{\mathcal{G}}(k) = \frac{\hat{\bar{\mathcal{G}}}(k)}{\bar{\mathcal{G}}(k)} = \cos(k\bar{\Delta}/2). \tag{D.10}$$

Therefore, the test filter in the physical space is simply the discrete arithmetic mean filter [48]:

$$\hat{G}(x) = \frac{1}{2} \left(\delta(x + \bar{\Delta}/2) + \delta(x - \bar{\Delta}/2) \right), \tag{D.11}$$

which amounts to taking the average between the two points located at a distance $\bar{\Delta}/2$. The extension to the present 3-D case is

$$\hat{G}(x,y,z) = \frac{1}{8} \left(\delta(x + \bar{\Delta}/2) + \delta(x - \bar{\Delta}/2) \right) \left(\delta(y + \bar{\Delta}/2) + \delta(y - \bar{\Delta}/2) \right) \times \left(\delta(z + \bar{\Delta}/2) + \delta(z - \bar{\Delta}/2) \right). \tag{D.12}$$

In a coarse-grid simulation, the filter size is typically considered to be twice the grid size Δ_G, i.e.

$$\bar{\Delta} = 2\Delta_G. \tag{D.13}$$

The test filtered quantity $\hat{\bar{\psi}}$ will thus be evaluated from the coarse-grid quantity $\bar{\psi}$ by taking the mean value of its 8 neighbors located on the corners of the cube of size Δ_G,

$$\hat{\bar{\psi}}_{ijk} = \frac{1}{8} \left(\bar{\psi}_{i+1,j+1,k+1} + \bar{\psi}_{i+1,j+1,k-1} + \bar{\psi}_{i+1,j-1,k+1} + \psi_{i+1,j-1,k-1} + \bar{\psi}_{i-1,j+1,k+1} + \bar{\psi}_{i-1,j+1,k-1} + \bar{\psi}_{i-1,j-1,k+1} + \bar{\psi}_{i-1,j-1,k-1} \right). \tag{D.14}$$

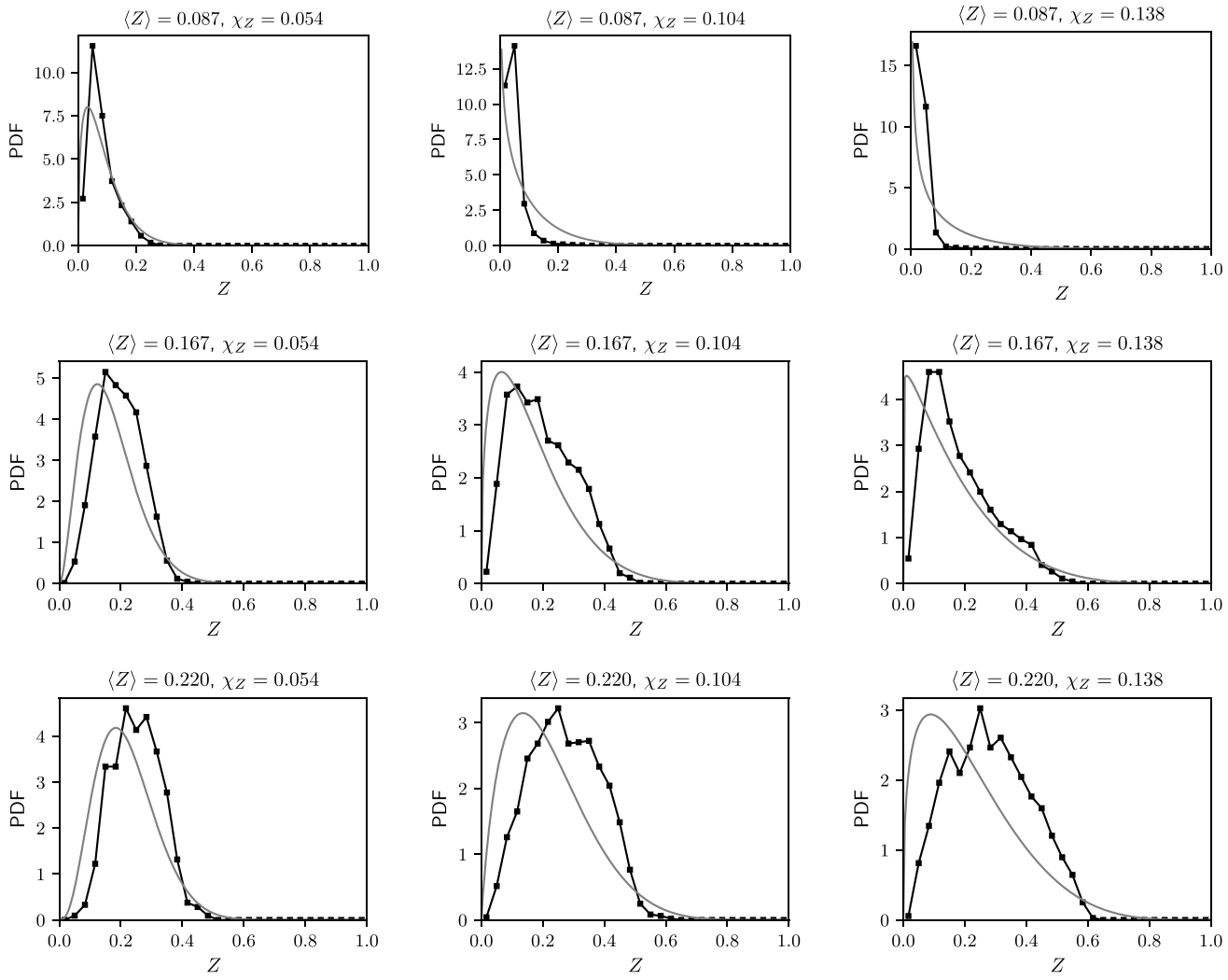

Fig. E.21. Conditional probability density function $P(Z|\langle Z\rangle, \chi_Z)$ for different values of $\langle Z\rangle$ and χ_Z (▬); presumed Beta distribution (—) function, $Fr_{\Delta}^{-1} = 0.486$.

Appendix E. Presumed sub-grid probability density function

As detailed in Section 5, the function f that appears in the new drift velocity model (Eq. (23)) can be fairly well approximated by a function of the first two filtered moments of the particle volume fraction. In addition, this approximate function f^* can be straightforwardly evaluated by conditional averaging like in previous functional approaches, without explicit dependency on the filter width.

Another strategy is to directly evaluate the model in Eq. (23) by closing the sub-grid moment $\left\langle \frac{\alpha_p^2}{\alpha_g} \right\rangle$ as a function of $\langle \alpha_p \rangle$ and $\langle \alpha_p'^2 \rangle$. To do so, one needs to model the probability distribution of the particle volume fraction at the sub-grid scale, i.e. to determine the PDF of α_p conditioned by its first two filtered moments. Similar techniques have been used for some time in Large Eddy Simulations of turbulent reacting flows [49–51], where the PDF of the sub-grid mixing fraction is classically modeled by a Beta distribution. By analogy, we propose to model the PDF of α_p as

$$P(Z|a,b) = C\, Z^{a-1}(1-Z)^{b-1}, \tag{E.1}$$

where

$$Z \triangleq \frac{\alpha_p}{\alpha_{p,max}} \tag{E.2}$$

is the normalized particle volume fraction, bounded between 0 and 1, a and b are the two parameters of the distribution and C is a normalization constant defined as

$$C = \frac{1}{\int_0^1 Z^{a-1}(1-Z)^{b-1} dZ} = \frac{\Gamma(a+b)}{\Gamma(a)\Gamma(b)}, \tag{E.3}$$

where Γ is the Gamma function. The parameters a and b can be evaluated from the first two moments of the distribution as

$$a = \left(\frac{1}{\chi_Z} - 1\right)\langle Z\rangle \tag{E.4}$$

and

$$b = \left(\frac{1}{\chi_Z} - 1\right)(1-\langle Z\rangle), \tag{E.5}$$

where χ_Z is the scaled variance of Z, also bounded between 0 and 1,

$$\chi_Z = \frac{\langle Z'^2\rangle}{\langle Z\rangle(1-\langle Z\rangle)}. \tag{E.6}$$

with

$$\langle Z'^2\rangle = \langle Z^2\rangle - \langle Z\rangle^2 = \frac{\langle \alpha_p'^2\rangle}{\alpha_{p,max}^2}. \tag{E.7}$$

Fig. E.21 compares the PDF of the particle volume fraction measured from our fine-grid data and conditioned by $\langle Z\rangle$ and χ_Z to a presumed

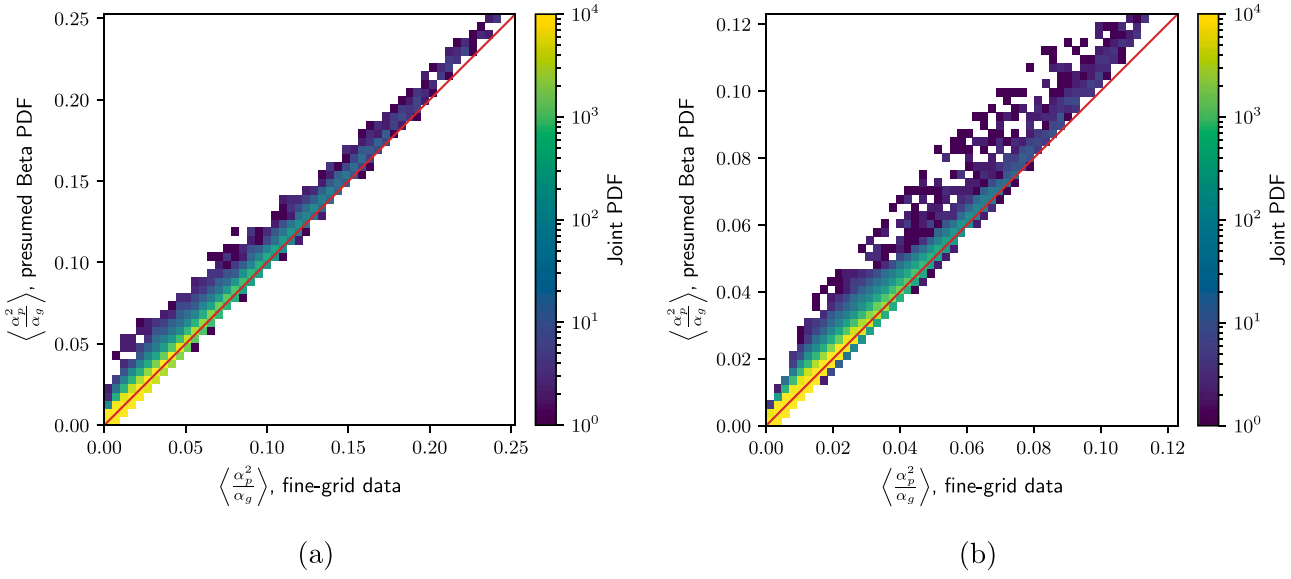

Fig. E.22. Correlation between the evaluation of the sub-grid moment $\left\langle \frac{\alpha_p^2}{\alpha_g} \right\rangle$ from a presumed Beta distribution and from our fine-grid data at (a) $Fr_{\tilde{\Delta}}^{-1} = 0.389$ ($R^2 = 0.994$) and (b) $Fr_{\tilde{\Delta}}^{-1} = 0.778$ ($R^2 = 0.990$).

Beta distribution whose parameters are determined from Eqs. (E.4) and (E.5), at a given filter width ($Fr_{\tilde{\Delta}}^{-1} = 0.486$). The agreement between the measured and presumed PDFs proves to be quite satisfactory, for various values of $\langle Z \rangle$ and χ_Z.

Finally, Fig. E.22 confirms that the unclosed sub-grid moment $\left\langle \frac{\alpha_p^2}{\alpha_g} \right\rangle$ can be successfully estimated from the presumed Beta distribution for two different filter widths (R^2 beyond 0.99 in both cases). Therefore, the model given by Eq. (23) can be effectively used in coarse-grid simulations if a closure is provided for the sub-grid variance of the particle volume fraction, $\left\langle \alpha_p'^2 \right\rangle$, as discussed in Section 5.

References

[1] M.A. van der Hoef, M. van Sint Annaland, N.G. Deen, J.A. Kuipers, Numerical simulation of dense gas-solid fluidized beds: A multiscale modeling strategy, Annu. Rev. Fluid Mech. 40 (1) (2008) 47–70, http://dx.doi.org/10.1146/annurev.fluid.40.111406.102130.

[2] H. Neau, M. Pigou, P. Fede, R. Ansart, C. Baudry, N. Mérigoux, J. Laviéville, Y. Fournier, N. Renon, O. Simonin, Massively parallel numerical simulation using up to 36,000 CPU cores of an industrial-scale polydispersed reactive pressurized fluidized bed with a mesh of one billion cells, Powder Technol. 366 (2020) 906–924, http://dx.doi.org/10.1016/j.powtec.2020.03.010.

[3] C.K. Lun, S.B. Savage, D.J. Jeffrey, N. Chepurniy, Kinetic theories for granular flow: Inelastic particles in Couette flow and slightly inelastic particles in a general flowfield, J. Fluid Mech. 140 (1984) 223–256, http://dx.doi.org/10.1017/S0022112084000586.

[4] J. Ding, D. Gidaspow, A bubbling fluidization model using kinetic theory of granular flow, AIChE J. 36 (4) (1990) 523–538, http://dx.doi.org/10.1002/aic.690360404.

[5] G. Balzer, A. Boelle, O. Simonin, Eulerian Gas Solid Flow Modelling of Dense Fluidized Bed, Tech. Rep., EDF - Electricité De France, 1995.

[6] K. Agrawal, P.N. Loezos, M. Syamlal, S. Sundaresan, The role of meso-scale structures in rapid gas-solid flows, J. Fluid Mech. 445 (3) (2001) 151–181, http://dx.doi.org/10.1017/s0022112001005663.

[7] J. Wang, A review of Eulerian simulation of Geldart A particles in gas-fluidized beds, Ind. Eng. Chem. Res. 48 (12) (2009) 5567–5577, http://dx.doi.org/10.1021/ie900247t.

[8] S. Sundaresan, Instabilities in fluidized beds, Annu. Rev. Fluid Mech. 35 (1948) (2003) 63–88, http://dx.doi.org/10.1146/annurev.fluid.35.101101.161151.

[9] J. Zhang, P. Jiang, L.-S. Fan, Flow characteristics of coal ash in a circulating fluidized bed, Ind. Eng. Chem. Res. 37 (4) (1998) 1499–1509, http://dx.doi.org/10.1021/ie970436w.

[10] A. Srivastava, K. Agrawal, S. Sundaresan, R.S. Karri, T.M. Knowlton, Dynamics of gas-particle flow in circulating fluidized beds, Powder Technol. 100 (2–3) (1998) 173–182, http://dx.doi.org/10.1016/S0032-5910(98)00138-7.

[11] A.T. Andrews, P.N. Loezos, S. Sundaresan, Coarse-grid simulation of gas-particle flows in vertical risers, Ind. Eng. Chem. Res. 44 (16) (2005) 6022–6037, http://dx.doi.org/10.1021/ie0492193.

[12] Y. Igci, A.T. Andrews, S. Sundaresan, S. Pannala, T. O'Brien, Filtered two-fluid models for fluidized gas-particle suspensions, AIChE J. 54 (6) (2008) 1431–1448, http://dx.doi.org/10.1002/aic.11481.

[13] J. Wang, M.A. van der Hoef, J.A. Kuipers, Coarse grid simulation of bed expansion characteristics of industrial-scale gas-solid bubbling fluidized beds, Chem. Eng. Sci. 65 (6) (2010) 2125–2131, http://dx.doi.org/10.1016/j.ces.2009.12.004.

[14] J.-F. Parmentier, O. Simonin, O. Delsart, A functional subgrid drift velocity model for filtered drag prediction in dense fluidized bed, AIChE J. 58 (4) (2012) 1084–1098, http://dx.doi.org/10.1002/aic.12647.

[15] A. Ozel, P. Fede, O. Simonin, Development of filtered Euler-Euler two-phase model for circulating fluidised bed: High resolution simulation, formulation and a priori analyses, Int. J. Multiph. Flow 55 (2013) 43–63, http://dx.doi.org/10.1016/j.ijmultiphaseflow.2013.04.002.

[16] Y. Igci, S. Sundaresan, Constitutive models for filtered two-fluid models of fluidized gas-particle flows, Ind. Eng. Chem. Res. 50 (23) (2011) 13190–13201, http://dx.doi.org/10.1021/ie200190q.

[17] S. Schneiderbauer, S. Puttinger, S. Pirker, Comparative analysis of subgrid drag modifications for dense gas-particle flows in bubbling fluidized beds, AIChE J. 59 (11) (2013) 4077–4099, http://dx.doi.org/10.1002/aic.14155.

[18] T.J. O'Brien, M. Syamlal, Particle cluster effects in the numerical simulation of a circulating fluidized bed, Circ. Fluid. Bed Technol. IV (1993) 367–372.

[19] T. McKeen, T. Pugsley, Simulation and experimental validation of a freely bubbling bed of FCC catalyst, Powder Technol. 129 (1–3) (2003) 139–152, http://dx.doi.org/10.1016/S0032-5910(02)00294-2.

[20] J. Gao, J. Chang, C. Xu, X. Lan, Y. Yang, CFD simulation of gas solid flow in FCC strippers, Chem. Eng. Sci. 63 (7) (2008) 1827–1841, http://dx.doi.org/10.1016/j.ces.2007.12.009.

[21] M. Ye, J. Wang, M.A. van der Hoef, J.A. Kuipers, Two-fluid modeling of Geldart A particles in gas-fluidized beds, Particuology 6 (6) (2008) 540–548, http://dx.doi.org/10.1016/j.partic.2008.07.005.

[22] J. Li, M. Kwauk, Particle-Fluid Two-Phase Flow: The Energy-Minimization Multi-Scale Method, Metallurgical Industry Press, Beijing, 1994.

[23] B. Lu, W. Wang, J. Li, Eulerian simulation of gas-solid flows with particles of Geldart groups A, B and D using EMMS-based meso-scale model, Chem. Eng. Sci. 66 (20) (2011) 4624–4635, http://dx.doi.org/10.1016/j.ces.2011.06.026.

[24] J. Wang, Y. Liu, EMMS-based Eulerian simulation on the hydrodynamics of a bubbling fluidized bed with FCC particles, Powder Technol. 197 (3) (2010) 241–246, http://dx.doi.org/10.1016/j.powtec.2009.09.022.

[25] Y. Igci, S. Pannala, S. Benyahia, S. Sundaresan, Validation studies on filtered model equations for gas-particle flows in risers, Ind. Eng. Chem. Res. 51 (4) (2012) 2094–2103, http://dx.doi.org/10.1021/ie2007278.

[26] C.C. Milioli, F.E. Milioli, W. Holloway, K. Agrawal, S. Sundaresan, Filtered two-fluid models of fluidized gas-particle flows: New constitutive relations, AIChE J. 59 (9) (2013) 3265–3275, http://dx.doi.org/10.1002/aic.14130.

[27] A. Sarkar, F.E. Milioli, S. Ozarkar, T. Li, X. Sun, S. Sundaresan, Filtered sub-grid constitutive models for fluidized gas-particle flows constructed from 3-D simulations, Chem. Eng. Sci. 152 (2016) 443–456, http://dx.doi.org/10.1016/j.ces.2016.06.023.

[28] S. Cloete, J.H. Cloete, S. Amini, Hydrodynamic validation study of filtered Two Fluid Models, Chem. Eng. Sci. 182 (2018) 93–107, http://dx.doi.org/10.1016/j.ces.2018.02.032.

[29] X. Gao, T. Li, A. Sarkar, L. Lu, W.A. Rogers, Development and validation of an enhanced filtered drag model for simulating gas-solid fluidization of Geldart A particles in all flow regimes, Chem. Eng. Sci. 184 (2018) 33–51, http://dx.doi.org/10.1016/j.ces.2018.03.038.

[30] M. Germano, U. Piomelli, P. Moin, W.H. Cabot, A dynamic subgrid-scale eddy viscosity model, Phys. Fluids A 3 (7) (1991) 1760–1765, http://dx.doi.org/10.1063/1.857955.

[31] R.O. Fox, On multiphase turbulence models for collisional fluid-particle flows, J. Fluid Mech. 742 (2014) 368–424, http://dx.doi.org/10.1017/jfm.2014.21.

[32] J. Capecelatro, O. Desjardins, R.O. Fox, Numerical study of collisional particle dynamics in cluster-induced turbulence, J. Fluid Mech. 747 (2014) R2, http://dx.doi.org/10.1017/jfm.2014.194.

[33] J. Capecelatro, O. Desjardins, R.O. Fox, Strongly coupled fluid-particle flows in vertical channels. II. Turbulence modeling, Phys. Fluids 28 (3) (2016) 033307, http://dx.doi.org/10.1063/1.4943234.

[34] S. Schneiderbauer, A spatially-averaged two-fluid model for dense large-scale gas-solid flows, AIChE J. 63 (8) (2017) 3544–3562, http://dx.doi.org/10.1002/aic.15684.

[35] S. Rauchenzauner, S. Schneiderbauer, A dynamic anisotropic Spatially-Averaged Two-Fluid Model for moderately dense gas-particle flows, Int. J. Multiph. Flow 126 (2020) 103237, http://dx.doi.org/10.1016/j.ijmultiphaseflow.2020.103237.

[36] S. Rauchenzauner, S. Schneiderbauer, A dynamic multiphase turbulence model for coarse-grid simulations of fluidized gas-particle suspensions, Chem. Eng. Sci. 247 (2022) 117104, http://dx.doi.org/10.1016/j.ces.2021.117104.

[37] A. Ozel, Y. Gu, C.C. Milioli, J. Kolehmainen, S. Sundaresan, Towards filtered drag force model for non-cohesive and cohesive particle-gas flows, Phys. Fluids 29 (10) (2017) http://dx.doi.org/10.1063/1.5000516.

[38] Y. Jiang, J. Kolehmainen, Y. Gu, Y.G. Kevrekidis, A. Ozel, S. Sundaresan, Neural-network-based filtered drag model for gas-particle flows, Powder Technol. 346 (2019) 403–413, http://dx.doi.org/10.1016/j.powtec.2018.11.092.

[39] Y. Jiang, X. Chen, J. Kolehmainen, I.G. Kevrekidis, A. Ozel, S. Sundaresan, Development of data-driven filtered drag model for industrial-scale fluidized beds, Chem. Eng. Sci. 230 (2021) 116235, http://dx.doi.org/10.1016/j.ces.2020.116235.

[40] J. De Wilde, Reformulating and quantifying the generalized added mass in filtered gas-solid flow models, Phys. Fluids 17 (11) (2005) 1–14, http://dx.doi.org/10.1063/1.2131925.

[41] D.Z. Zhang, W.B. VanderHeyden, The effects of mesoscale structures on the macroscopic momentum equations for two-phase flows, Int. J. Multiph. Flow 28 (5) (2002) 805–822, http://dx.doi.org/10.1016/S0301-9322(02)00005-8.

[42] S. Schneiderbauer, M. Saeedipour, Approximate deconvolution model for the simulation of turbulent gas-solid flows: An a priori analysis, Phys. Fluids 30 (2) (2018) 3544–3562, http://dx.doi.org/10.1063/1.5017004.

[43] F. Gao, E.E. O'Brien, A large-eddy simulation scheme for turbulent reacting flows, Phys. Fluids A 5 (6) (1992) 1282–1284, http://dx.doi.org/10.1063/1.858617.

[44] S. Radl, S. Sundaresan, A drag model for filtered Euler-Lagrange simulations of clustered gas-particle suspensions, Chem. Eng. Sci. 117 (2014) 416–425, http://dx.doi.org/10.1016/j.ces.2014.07.011.

[45] S. Sundaresan, S. Radl, C.C. Milioli, F.E. Milioli, Coarse-Grained models for momentum, energy and species transport in gas-particle flows, in: The 14th International Conference on Fluidization – from Fundamentals To Products, 2013.

[46] C. Wen, Y. Yu, Mechanics of Fluidization, in: Chemical Engineering Symposium Series, Vol. 62, 1966, pp. 100–111.

[47] D.K. Lilly, A proposed modification of the Germano subgrid-scale closure method, Phys. Fluids A 4 (3) (1992) 633–635, http://dx.doi.org/10.1063/1.858280.

[48] G.S. Winckelmans, A.A. Wray, O.V. Vasilyev, H. Jeanmart, Explicit-filtering large-eddy simulation using tensor-diffusivity model supplemented by a dynamic smagorinsky term, Phys. Fluids 13 (5) (2001) 1385–1403, http://dx.doi.org/10.1063/1.1360192.

[49] R.W. Bilger, Turbulent flows with nonpremixed reactants, in: P.A. Libby, F.A. Williams (Eds.), Turbulent Reacting Flows, Springer Berlin Heidelberg, 1980, pp. 65–113, http://dx.doi.org/10.1007/3540101926_9.

[50] F.A. Maury, P.A. Libby, Nonpremixed flames in stagnating turbulence part I - The k-ϵ theory with equilibrium chemistry for the methane-air system, Combust. Flame 102 (3) (1995) 341–356, http://dx.doi.org/10.1016/0010-2180(94)00280-6.

[51] C. Wall, B.J. Boersma, P. Moin, An evaluation of the assumed beta probability density function subgrid-scale model for large eddy simulation of nonpremixed, turbulent combustion with heat release, Phys. Fluids 12 (10) (2000) 2522–2529, http://dx.doi.org/10.1063/1.1287911.